Energy Conversion and Management: X 21 (2024) 100516

Contents lists available at ScienceDirect

Energy Conversion and Management: X

journal homepage: www.sciencedirect.com/journal/energy-conversion-and-management-x

Thermo-economic assessment and optimization of an innovative tri-generation system using supercritical CO_2 power system and LNG cold energy recovery

Mohamed S. Yousef [a,b,*], Domingo Santana [a]

[a] Department of Thermal and Fluids Engineering, Carlos III University of Madrid, Avda. de la Universidad 30, 28911 Leganés, Madrid, Spain
[b] Department of Mechanical Engineering, Benha Faculty of Eng., Benha University, Benha, Egypt

ARTICLE INFO

Keywords:
sCO_2 cycle
LNG
Kalina cycle
ORC
ARC
Hydrogen

ABSTRACT

The present study introduces a novel tri-generation system that is highly efficient and cost-effective, employing a supercritical CO_2 (sCO_2) Brayton cycle as the primary mover and harnessing the cooling potential from liquefied natural gas (LNG) as a heat sink. This innovative system simultaneously provides electricity, cooling, and hydrogen. By capitalizing on the substantial temperature difference between the high-temperature sCO_2 power cycle and the low-temperature LNG cold source, an integrated combination of the Kalina cycle (KC) and organic Rankine cycle (ORC) is utilized. Additionally, the system incorporates a proton exchange membrane electrolyzer (PEME) and an absorption refrigeration cycle (ARC) to create a highly efficient trigeneration system. The system is rigorously evaluated through energy, exergy, and exergoeconomic analyses, which are critical for assessing performance. Additionally, this study conducts a parametric investigation to elucidate the impact of key parameters on system performance. Furthermore, optimization is performed using a genetic algorithm (GA), with the objective of maximizing energy and exergy efficiencies or minimizing the overall product cost. Results from the baseline scenario demonstrate impressive energy and exergy efficiencies of 54.38 % and 59.46 % respectively, along with a low total product unit cost of 11.642 ($/GJ), outperforming existing benchmarks in the literature. The system also provides substantial net power output, cooling capacity, and hydrogen production rates of 276.71 MW, 60.19 MW, and 176.25 kg/h, respectively. This combination of high performance and cost-effectiveness makes the proposed system a versatile choice, underscoring its significance in sustainable and environmentally friendly energy solutions.

Introduction

The urgent need to transition away from fossil fuels and address environmental concerns has highlighted the importance of clean energy, reduced emissions, and enhanced energy efficiency [1]. The supercritical carbon dioxide (sCO_2) Brayton cycle emerges as a promising solution, offering environmental sustainability and adaptability across various heat sources [2]. Notably, advancements in Gen IV nuclear reactors emphasize the potential of nuclear energy, necessitating research to optimize sCO_2 cycles. However, efficient strategies for utilizing waste heat from sCO_2 power cycles remain a crucial focus. Amidst rising energy demands, combined energy systems employing the sCO_2 Brayton cycle have become a key area of intense study [3].

One promising approach is to tap into the wasted heat from gas coolers in sCO_2 power cycles to generate electricity [4]. This shift towards energy cascade utilization has researchers exploring the potential of absorption power cycles (APC), Organic Rankine Cycle (ORC), Kalina cycle (KC), and transcritical CO_2 cycle (tCO_2), to better harness low-grade waste heat [5]. In the study by Song et al. [6], two integrated sCO_2/ORC systems were compared, one incorporating a pre-cooler in the topping cycle and the other without. The research revealed that without a pre-cooler, the ORC system could capture all waste heat, maximizing energy efficiency. However, this approach limited thermodynamic performance improvements due to the lower evaporation temperature. Conversely, with a pre-cooler, only partial waste heat utilization occurred, but it led to higher evaporation temperatures in the ORC, offering greater benefits for bottoming cycles. In their study, Wu

* Corresponding author at: Department of Thermal and Fluids Engineering, Carlos III University of Madrid, Avda. de la Universidad 30, 28911 Leganés, Madrid, Spain.
E-mail address: myousef@ing.uc3m.es (M.S. Yousef).

https://doi.org/10.1016/j.ecmx.2023.100516
Received 19 October 2023; Received in revised form 4 December 2023; Accepted 17 December 2023
Available online 18 December 2023
2590-1745/© 2023 The Authors. Published by Elsevier Ltd. This is an open access article under the CC BY-NC-ND license (http://creativecommons.org/licenses/by-nc-nd/4.0/).

Nomenclature

A	Heat transfer area (m^2)
$\dot{C}$	Cost rate ($/h)
c	Cost per exergy unit ($/GJ)
$c_{P,total}$	Total product unit cost ($/GJ)
$\dot{E}$	Exergy rate (kW)
e	Standard chemical exergy (kJ/kg)
F	Faraday constant (c/mol)
f_k	Exergoeconomic factor
h	Specific enthalpy (kJ/kg)
i	Interest rate
J	Current density (A/m^2)
LMTD	Log mean temperature difference (°C)
$\dot{m}$	mass flow rate (kg/s)
M	Molar mass (kg/kmol)
n	Number of operation year
P	Pressure (bar) & (kPa)
PRc	Compressor pressure ratio
$\dot{Q}$	Heat transfer rate (kW)
R	Overall ohmic resistance, (Ω)
r_k	Relative cost difference
s	specific entropy (kJ/kg K)
T	Temperature (°C) & Turbine
U	Overall heat transfer coefficient (W/m^2K)
V	Voltage
$\dot{W}$	Power (kW)
X	Ammonia mass fraction (%)
Z	Capital cost of a component ($)
$\dot{Z}$	Capital cost rate ($/h)

Greek symbols

η	Efficiency (%)
ϵ	Effectiveness
Δ	Difference
τ	Annual plant operation Hours (h)
γ	Maintenance factor
M	Entrainment ratio
λ	Content of water
Σ	Total ionic conductivity

Subscripts and abbreviations

0	Ambient state
APC	Absorption Power Cycle
act	activation
CRF	Capital recovery factor
CCP	Combined cooling and power system
COND	Condenser
ch	Chemical
c	Cathode
COD	Cost optimal design
d	Destruction
EES	Engineering Equation Solver
ERC	Ejector refrigeration cycle
evap	Evaporator
E.V1	Expansion valve 1
E.V2	Expansion valve 2
E.V3	Expansion valve 3
EVAP	Evaporator
EEOD	Energy efficiency optimal design
ex	Exergy
exi	exit
F	Fuel
Gen1	Generator1
Gen2	Generator2
HTR	High temperature recuperator
HEX	Heat exchanger
H_2	Hydrogen
Gen2,hot	Hot end temperature difference for generator2
in	Inlet
KC	Kalina cycle
k	Component number
LTR	Low temperature recuperator
LiBr	Lithium bromide
LNG	Liquefied natural gas
L	loss
MC	Main compressor
ORC	Organic Rankine cycle
OM	Operation and maintenance
ohm	ohmic
out	outlet
PC	Pre-cooler
P	Product
PEME	Proton exchange membrane electrolysis
RC	Recompression compressor
R	Reactor
ref	reference
SCRBC	supercritical CO_2 recompression Brayton
SR	Split ratio
SHX	Solution heat exchanger
TUR1	sCO_2 Turbine
TUR2	KC Turbine
TUR3	ORC Turbine
TUR4	NG Turbine
tot	Total
TTD	Terminal temperature difference
tCO_2	Transcritical CO_2 cycle
V.G1	Vapor generator1
V.G2	Vapor generator2
XEOD	Exergy efficiency optimal design

et al. [7] analyzed the SCRBC/OFC, a system that combines supercritical carbon dioxide recompression Brayton cycle and organic flash cycle. This system utilizes the waste heat from the SCRBC to generate power. The researchers found that the exergy efficiency of the SCRBC/OFC was 6.57 % higher, and the total product unit cost was 3.57 % lower compared to the SCRBC. By comparing a cascade cycle with sCO_2 recompression as the topping and ORC with isobutene working fluid in the bottoming, Wang and Dai [8] discovered an exergetic efficiency of up to 62.64 %.

The ammonia-water mixture stands out in Kalina Cycle (KC) designs for power generation due to distinct advantages over organic fluids, leading to increased attention. Its noteworthy thermodynamic characteristics, including a temperature glide feature uncommon in most azeotropic mixtures, make it a versatile working fluid capable of undergoing phase changes across a broad temperature range [9]. This unique property enhances thermodynamic matching with heat sources, making the ammonia-water system particularly suitable for applications in low-grade heat recovery [10]. Through an extensive comparative study, Shokati et al. [11] found that the KC was most cost-effective for energy production when compared to a simple ORC system using 175 °C heat source. Optimized results showed key advantages of up to 66 % in unit produced power at reduced costs, making it one of the best options

for waste heat recovery. Studies have explored the recuperation of waste heat from sCO_2 cycles using a KC. Li et al. and Mahmoudi et al. [12,13] both concluded that combining a supercritical carbon dioxide recompression Brayton cycle (SCRBC) with KC produces significantly better results, such as lower total product unit cost and higher exergy efficiency than those of single SCRBC tied to no other system; specifically 4.9–5.5 % more efficient in terms of productivity costs and 8–10 % increased effectiveness relative to exergy output when compared against standalone cycles.

Incorporating the sCO_2 cycle into various power generation systems has demonstrated a substantial improvement in energy efficiency. However, the implementation of combined cooling and power (CCP) systems emerges as an exceptionally promising strategy to further elevate the performance of the sCO_2 systems. CCP systems not only produce power but also deliver cooling, thereby amplifying the efficiency and sustainability of the sCO_2 technology [14]. Yuan et al. [15] examined a distributed energy system and uncovered a noteworthy cost increase in product units when transitioning from full power mode to full refrigeration mode. Li and Wang [16] uncovered a method of significantly improving the exergy efficiency in a new CCP system by connecting an SCRBC to a tCO_2 refrigeration cycle. Their findings revealed that CCP system performance could be enhanced between 2.45 and 5.87 % when operating within evaporation temperatures of 20 °C–0 °C, compared to standalone cooling and power solutions. Pan et al. [17] introduced a novel CCP system that effectively utilizes engine waste heat. Comprising a regenerative sCO_2 Brayton cycle (RSCBC) for power generation and an ejector expansion refrigeration cycle (EERC) for refrigeration. The study delved into the evaluation of diverse zeotropic mixtures in the EERC through energy and exergy analysis, discussing the influence of varied operational factors. Notably, employing a specific R32/CO_2 mixture, the system attained an impressive refrigerating capacity of 225.5 kW along with a COP of 2.05.

Absorption refrigeration cycles (ARCs) are widely employed for energy utilization, harnessing low-grade heat for cooling benefits [18]. Ammonia-water (NH_3-H_2O) and lithium bromide-water (LiBr-H_2O) are common working pairs, with ammonia serving as the refrigerant in one cycle, and water used for its lower evaporation temperature in another [19]. While ARCs driven by higher temperatures (50–200 °C) exhibit superior performance, LiBr-H_2O ARCs are preferred for efficiency due to smaller component volumes, operating within the 75–110 °C range [20]. ARCs outperform ejector refrigeration cycles (ERCs) in cooling production, offering higher coefficient of performance (COP), enhanced energy efficiency, reduced electricity usage, quiet operation, simplified designs, and flexibility in heat sources [21]. Integrating ARCs with sCO_2 power cycles in CCP systems emerges as an inventive strategy to boost efficiency by utilizing surplus cooling heat from nuclear power plants [22]. Wu et al. [23] undertook a comprehensive comparison between the stand-alone a SCRBC cycle and one enhanced with NH_3-H_2O, revealing that the amalgamated system exhibited superior thermodynamic and exergoeconomic performance. This outcome prompted further exploration of additional alternatives, such as LiBr-H_2O refrigeration systems, which have proven advantageous in specific conditions compared to NH_3-H_2O. In a recent study, Wu et al. [24] presented an innovative approach for a CCP system. It integrates distinct features of the regenerative sCO_2 cycle with an NH_3-H_2O ARC. The proposed CCP system demonstrates significant improvements, including a rise in exergy efficiency by up to 2.54 % and a boost in thermal efficiency by 18.93 %.

Liquid natural gas (LNG) is gaining traction for multi-generation systems, cutting costs through efficient waste heat recovery. It offers easy transport, stable storage without re-liquefaction, and high energy density. Integrated into power grids, LNG taps into valuable cold energy from regasification, reducing emissions and saving costs [25]. Utilizing LNG cold exergy recovery in power augmentation produces clean energy for diverse locations, optimizing electricity generation. Compared to other fuels, LNG provides substantial environmental benefits by reducing emissions. The popularity of harnessing LNG's cold source through low-temperature heat cycles is on the rise [26]. Ebadollahi et al. [27] developed a poly-generation system powered by geothermal energy, featuring an ORC, ERC, and a PEME (Proton Exchange Membrane Electrolyzer), and an LNG-based power generation facility. Analysis of the model provided remarkable results for each component; with respective efficiencies standing at 38.3 %, 28.9 % and 347$/GJ in terms of energy, exergy and total unit product cost respectively. Ghaebi et al. [28] have introduced an innovative approach to harness the renewable energy potential of geothermal power and LNG as a heat sink. They employed the cost-effective and highly efficient KC-KC integrated system, achieving an impressive peak performance level approaching 43 %. Their study successfully achieved optimal efficiency rates at remarkably low costs, as low as 127 $/GJ. Chitgar and Moghimi [29] proposed an inventive waste heat recovery solution involving a KC, an ORC, and an LNG-based power generation unit. This integrated system achieved an impressive exergetic efficiency of 54.4 %, all at a cost-effective rate of 24.6$/GJ.

Hydrogen is a key player in sustainable energy solutions, especially for multi-generation systems. It offers eco-friendly energy but faces challenges due to limited natural abundance and emissions from traditional methane-based production. To address these concerns, cleaner alternatives like water electrolysis, photo-catalysis, and thermochemical processes are gaining traction. Electrolysis, in particular, stands out as an efficient and scalable choice. Notably, exploring hydrogen production from environmentally friendly sources like nuclear-based sCO_2 power cycles receives little attention in current literature. Abid et al. [30] focused on enhancing solar collector performance and hydrogen production. The researchers integrated a parabolic dish solar collector into a SCRBC, yielding impressive outcomes. The results indicated that the reheat-enabled system exhibited superior overall efficiencies, rendering it a favorable option for hydrogen production. Hadelu et al. [31] proposed a solar-based multi-generation system utilizing solar energy for power generation, cooling, distilled water production, and hydrogen generation. Comprising a sCO_2 power cycle, solar distillation unit, and an electrolyzer integrated with parabolic dish collectors. They conducted a comprehensive evaluation of a range of phase change materials, leading to the identification of Cu-Si as the leader in terms of thermodynamic performance.

This study presents an innovative tri-generation system designed to provide power, cooling, and hydrogen production simultaneously. The core concept involves employing a nuclear-driven sCO_2 power cycle as a high-temperature heat source and harnessing the cold energy from LNG as a low-temperature heat sink. This innovative design not only introduces a novel system configuration but also pursues the dual goals of enhancing overall system efficiency and providing reliable, sustainable energy solutions. The suggested system consists of several key components, including a unique cascade setup, a PEME, and an ARC system. Within the cascade setup, the sCO_2 power cycle, a KC, an ORC, and an LNG subsystem work synergistically. The power generated by the KC is harnessed for hydrogen production in the PEME. Notably, the configuration presented in this study is a novel one. Despite an extensive review of existing literature, there is no record of an analysis of a tri-generation system utilizing a nuclear-based sCO_2 power cycle as the primary heat source and LNG cold energy as the primary cooling resource in this specific arrangement. Addressing these research gaps, our study aims to provide a comprehensive and unprecedented system capable of efficiently and cost-effectively producing power, cooling, and hydrogen simultaneously, thereby enhancing overall system efficiency and offering reliable, sustainable energy solutions.

The primary aims of this study can be succinctly summarized as follows:

- Introduce a novel tri-generation system configuration that incorporates a nuclear-based sCO_2 power cycle as a heat source and

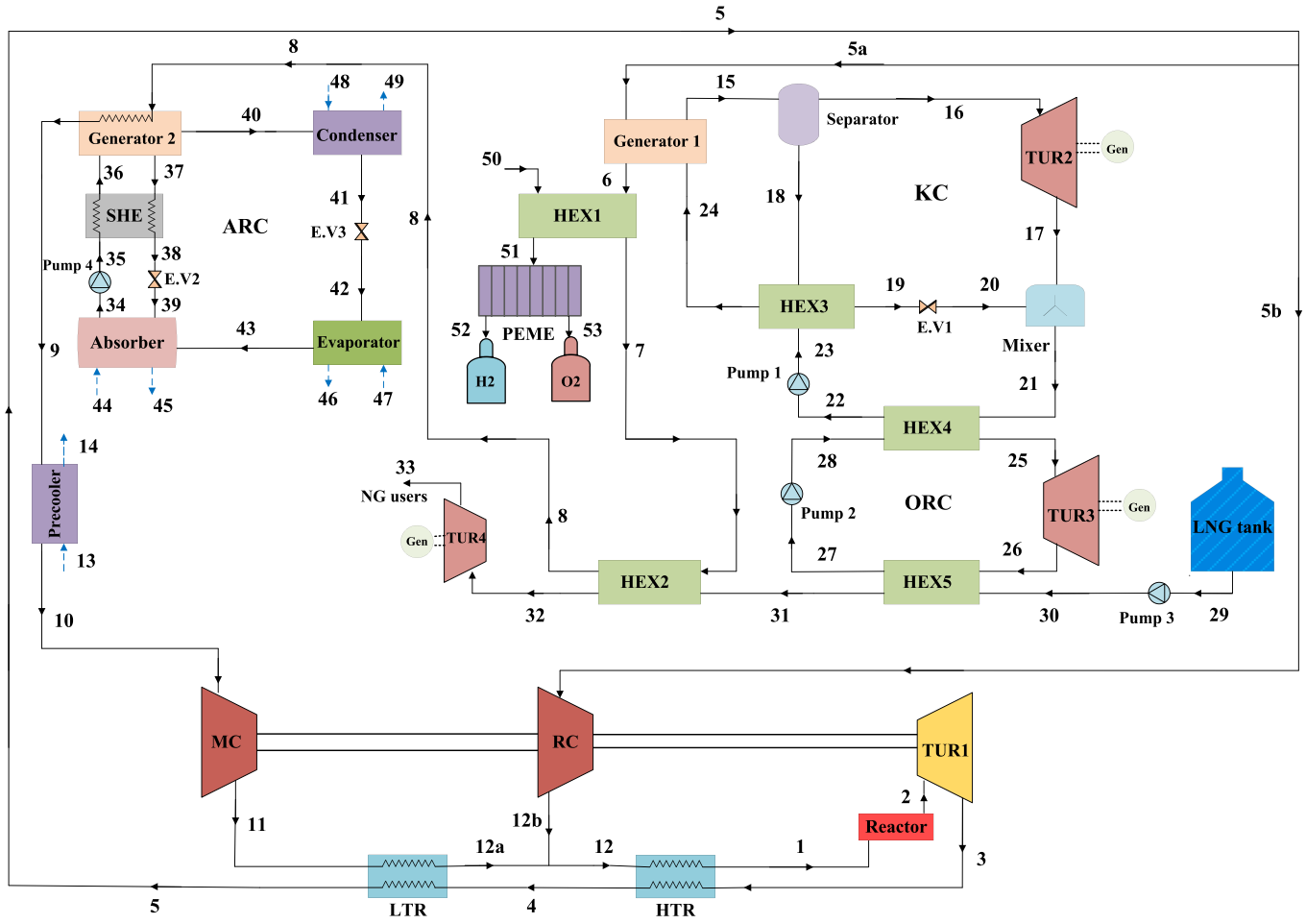


Fig. 1. A schematic diagram of the proposed trigeneration system.

LNG as the heat sink, enabling power, cooling, and hydrogen production.

- Conduct a thorough examination of the proposed system, considering energy, exergy, and exergoeconomic viewpoints.
- Perform an extensive parametric study to evaluate the impact of various parameters on the system's thermodynamic and economic performance.
- Optimize the proposed system using a genetic algorithm (GA) in three scenarios: maximizing energy efficiency (η_{en}), exergy efficiency (η_{ex}), or minimizing overall product cost ($c_{P;tot}$).

System description

Fig. 1 illustrates the schematic diagram of the proposed trigeneration system, which incorporates various components. These include a recompression sCO_2 power cycle (SCRBC), coupled with various subsystems such as a cascade power cycle involving KC and ORC power systems, an LNG heat sink, a PEME unit, and an ARC. The cycle combines the SCRBC with these subsystems, enabling the use of heat rejected from the SCRBC pre-cooler to power the other systems. The SCRBC is comprised of several key components, namely the main compressor (MC), low temperature recuperator (LTR), reactor, high temperature recuperator (HTR), sCO_2 turbine (TUR1), recompression compressor (RC), and pre-cooler (PC). Additionally, the KC power cycle includes vapor generator 1 (VG1), separator, Kalina turbine (TUR2), heat exchanger 3 (HEX3), expansion valve (EV1), pump1, mixer, and heat exchanger 4 (HEX4), which is shared with the bottoming ORC power cycle. The ORC power cycle consists of pump2, ORC turbine (TUR3), and heat exchanger 5 (HEX5). Furthermore, the LNG heat sink subsystem is composed of an LNG tank, pump3, heat exchanger 2 (HEX2), and NG turbine (TUR4). The hydrogen production subsystem includes heat exchanger 1 (HEX1) and the PEME unit. Finally, the ARC encompasses vapor generator 2 (VG2), solution heat exchanger (SHX), pump 4, throttling valve (TV2), absorber, evaporator, throttling valve (TV3), and a condenser.

The journey of CO_2 within the system is as follows: CO_2 exits the PC and enters the MC for pressurization. Initially, the CO_2 stream undergoes preheating within the LTR before combining with the stream exiting the RC at state 12. This combined blend is further heated in the HTR, goes through a phase change in the reactor, and experiences expansion within TUR1. The expanded flow is then directed back to the HTR to provide heat to the flow at state 12 and subsequently to the LTR for heating the flow at state 11. Upon reaching the exit of the LTR (designated as point 5), the CO_2 stream is split into two separate paths: stream 5a and stream 5b. Flow 5a enters the VG1, where it transfers a fraction of its energy to the KC, and then proceeds to HEX1 to raise the temperature of incoming water before entering the PEME. Meanwhile, stream 5b undergoes compression in the RC and is subsequently combined with the CO_2 from the LTR.

In the KC, the ammonia-water mixture undergoes a crucial transformation. As it flows through VG1, this mixture transitions into a two-phase fluid. Subsequently, it encounters a separator where it's divided into two distinct phases: saturated vapor and saturated liquid. The saturated vapor stream proceeds to TUR2 to harness power, while the saturated liquid flow from the separator enters HX3 to preheat the outgoing stream from Pump 1. Following this, the working fluid

Table 1
Thermodynamic balance equations for components in the proposed trigeneration system.

Component	Equation
MC	$\dot{W}_{MC} = (1-SR)\dot{m}_{CO2}(h_{11}-h_{10}), h_{11} = h_{10} + (h_{11s}-h_{10})/\eta_{MC}$
Reactor	$\dot{Q}_R = \dot{m}_{CO2}(h_2 - h_1)$
RC	$\dot{W}_{RC} = SR\,\dot{m}_{CO2}(h_{12}-h_5), h_{12} = h_5 + (h_{12s}-h_5)/\eta_{RC}$
LTR	$\dot{Q}_{LTR} = \dot{m}_{CO2}(h_4-h_5) = (1-SR)\dot{m}_{CO2}(h_{12}-h_{11}), \varepsilon_{LTR} = \frac{T_4-T_5}{T_4-T_{11}}$
sCO_2 turbine	$\dot{W}_{TUR1} = \dot{m}_{CO2}(h_2-h_3), h_3 = h_2-(h_2-h_{3s})\eta_{TUR1}$
HTR	$\dot{Q}_{HTR} = \dot{m}_{CO2}(h_3-h_4) = \dot{m}_{CO2}(h_1-h_{12}), \varepsilon_{HTR} = \frac{T_3-T_4}{T_3-T_{12}}$
Pre-cooler	$\dot{Q}_{PC} = (1-SR)\dot{m}_{CO2}(h_9-h_{10}) = \dot{m}_{PC}(h_{14}-h_{13})$
V.G 1	$\dot{Q}_{GEN1} = (1-SR)\dot{m}_{CO2}(h_{5a}-h_6) = \dot{m}_{15}(h_{15}-h_{24})$ $TTD_{Gen1} = T_{5a}-T_{15}$
Separator	$\dot{m}_{15} = \dot{m}_{16} + \dot{m}_{18}, \dot{m}_{15}h_{15} = \dot{m}_{16}h_{16} + \dot{m}_{18}h_{18}$
H.EX 1	$\dot{Q}_{H.EX1} = \dot{m}_6(h_6-h_7) = \dot{m}_{50}(h_{51}-h_{50})$
H.EX 2	$\dot{Q}_{H.EX2} = \dot{m}_7(h_7-h_8) = \dot{m}_{31}(h_{32}-h_{31})$
H.EX 3	$\dot{Q}_{H.EX3} = \dot{m}_{18}(h_{18}-h_{19}) = \dot{m}_{23}(h_{24}-h_{23})$
KC turbine	$\dot{W}_{TUR2} = \dot{m}_{16}(h_{16}-h_{17}), h_{17} = h_{16}-(h_{16}-h_{17s})\eta_{TUR2}$
E.V1	$h_{19} = h_{20}$
Mixer	$\dot{m}_{17} + \dot{m}_{20} = \dot{m}_{21}, \dot{m}_{17}h_{17} + \dot{m}_{20}h_{20} = \dot{m}_{21}h_{21}$
Pump1	$\dot{W}_{PUMP1} = \dot{m}_{22}(h_{23}-h_{22}), \eta_{PUMP1} = (h_{23s}-h_{22})/(h_{23}-h_{22})$
H.EX 4	$\dot{Q}_{H.EX4} = \dot{m}_{21}(h_{21}-h_{22}) = \dot{m}_{28}(h_{25}-h_{28})$
ORC turbine	$\dot{W}_{TUR3} = \dot{m}_{25}(h_{25}-h_{26}), h_{26} = h_{25}-(h_{25}-h_{26s})\eta_{TUR3}$
Pump2	$\dot{W}_{PUMP2} = \dot{m}_{27}(h_{28}-h_{27}), \eta_{PUMP2} = (h_{28s}-h_{27})/(h_{28}-h_{27})$
H.EX 5	$\dot{Q}_{H.EX5} = \dot{m}_{26}(h_{26}-h_{27}) = \dot{m}_{30}(h_{31}-h_{30})$
Pump3	$\dot{W}_{PUMP3} = \dot{m}_{29}(h_{30}-h_{29}), \eta_{PUMP3} = (h_{30s}-h_{29})/(h_{30}-h_{29})$
LNG turbine	$\dot{W}_{TUR4} = \dot{m}_{32}(h_{32}-h_{33}), h_{33} = h_{32}-(h_{32}-h_{33s})\eta_{TUR4}$
V.G 2	$\dot{m}_{36} = \dot{m}_{37} + \dot{m}_{40}, \dot{m}_{36}X_{36} = \dot{m}_{37}X_{37},$ $\dot{Q}_{GEN1} = \dot{m}_8(h_8-h_9) = \dot{m}_{37}h_{37} + \dot{m}_{40}h_{40} - \dot{m}_{36}h_{36}$ $\Delta T_{hot,Gen2} = T_8 - T_{40}, \Delta T_{cold,Gen2} = T_9 - T_{36}$
Condenser	$\dot{Q}_{COND} = \dot{m}_{40}(h_{40}-h_{41}) = \dot{m}_{48}(h_{49}-h_{48})$
Evaporator	$\dot{Q}_{EVAP} = \dot{m}_{43}(h_{43}-h_{42}) = \dot{m}_{46}(h_{46}-h_{47})$
SHX	$\dot{Q}_{SHX} = \dot{m}_{35}(h_{36}-h_{35}) = \dot{m}_{37}(h_{38}-h_{37}),$ $\varepsilon_{SHX} = (T_{37}-T_{38})/(T_{37}-T_{35})$
Absorber	$\dot{Q}_{ABS} = \dot{m}_{39}h_{39} + \dot{m}_{43}h_{43} - \dot{m}_{34}h_{34} = \dot{m}_{44}(h_{45}-h_{44})$
Pump4	$\dot{W}_{PUMP4} = \dot{m}_{34}(h_{35}-h_{34}), \eta_{PUMP4} = (h_{35s}-h_{34})/(h_{35}-h_{34})$
T.V2	$h_{38} = h_{39}$
T.V3	$h_{41} = h_{42}$
PEME	Refer to electrolyzer modeling, as described in Section 3.2.

combines with the effluent from TUR2. Simultaneously, the waste heat from the NH_3-H_2O mixture is directed to HX4, where it is effectively recovered by Isobutane, which serves as the working fluid in the ORC. The power generated by TUR2 is subsequently consumed by the PEME for hydrogen production. An innovative feature of our system is the utilization of LNG as the heat rejection medium for the ORC, as opposed to traditional water cooling. This choice provides the opportunity to lower the ORC's temperature and pressure thresholds while simultaneously boosting its power generation. LNG, with its incredibly low temperature at −161.5 °C and atmospheric pressure, is directed into the pump and, after undergoing a pressure increase, transitions into saturated vapor as it passes through HX5. In the next stage, HX2 takes center stage by elevating the temperature of the natural gas. This increase in gas enthalpy at the inlet of TUR4 is achieved by harnessing the heat from the CO_2 stream 7 (located at the outlet of HX1) as a heat source. The gas exiting TUR4 is now ready for consumption by end-users, showcasing the efficiency and versatility of our system.

Stream 8 undergoes a transformative process as it passes through VG2, transferring waste heat to the ARC below. It then undergoes a crucial heat release process in a PC, designed to bring it close to its critical point temperature before entering the MC for compression. Within the lower-tier ARC system, Solution Point 36 experiences a significant heat influx from Stream 37 in VG2. This influx raises the temperature of the solution and initiates the separation of the refrigerant from the solution phase, resulting in the emergence of heated refrigerant, known as Steam 40. Steam 40 subsequently condenses into a saturated liquid state at Point 41 due to the cooling water. It is then subjected to throttling through TV3 and introduced into the evaporator, where it efficiently absorbs heat under low pressure, providing the necessary cooling energy for end-user needs. Simultaneously, the heated concentrated solution releases its stored heat within the SHX, undergoes controlled expansion across TV2, and is readily absorbed by Stream 39 in the evaporator. This harmonious blend cools and transitions into a saturated liquid state at Point 34. Finally, Stream 34 reaches the desired pressure level at Pump 4. Throughout this intricate and energy-efficient ARC cycle, Stream 34 diligently absorbs additional heat within the SHX and the generator, thereby concluding the process.

Mathematical models, performance assessment metrics, and assumptions

The thermodynamic and exergoeconomic characteristics of the envisioned system are meticulously evaluated through a simulation conducted using Engineering Equation Solver (EES). In this simulation, a comprehensive set of conservation equations encompassing mass, energy, and exergy, as well as exergoeconomic relationships, are meticulously formulated and implemented. For simplifying the modeling process, we make the following assumptions [32]:

- The proposed system operates within a state of equilibrium.
- Equipment like compressors, pumps, and turbines are typically assigned a constant isentropic efficiency.
- The pumps receive saturated liquid as their inlet flows, while the ORC turbine takes in saturated vapor as its inlet flow.
- The effluent streams from the evaporator, generator, condenser, and separator should be in a state of saturation.
- The kinetic and potential energy variations within the working fluid can be considered negligible.
- No pressure drop occurs within the components and connecting pipes.

Thermodynamic analysis

The thermodynamic models for the proposed trigeneration system have been meticulously developed by adhering to the fundamental principles of mass, energy, and exergy conservation. The following equations provide a comprehensive framework for this system [23]:

$$\sum \dot{m}_{in} = \sum \dot{m}_{out} \tag{1}$$

$$\sum \dot{m}_{in}X_{in} = \sum \dot{m}_{out}X_{out} \tag{2}$$

$$\sum \dot{Q} - \sum \dot{W} = \sum \dot{m}_{out}h_{out} - \sum \dot{m}_{in}h_{in} \tag{3}$$

Table 1 summarizes the thermodynamic balance equations associated with the components within the proposed trigeneration system, aiding in the analysis of system performance.

Table 2 presents a comprehensive array of exergy balance equations that correspond to each individual component within the proposed trigeneration system. The concept of overall exergy ($\dot{E}$) is meticulously dissected into its two constituent components: physical exergy ($\dot{E}_{ph}$) and chemical exergy ($\dot{E}_{ch}$), with the omission of any considerations for kinetic or potential energy fluctuations within the working fluid [33]. The inclusion or exclusion of chemical exergy calculations is contingent upon the constancy of the working medium's concentration throughout the process. In instances where the composition remains unaltered, such as with CO_2 within the topping subsystem, the chemical exergy can be disregarded. However, it is imperative to account for chemical exergy when variations in concentration occur during the process, exemplified by the NH_3-H_2O solution within the KC subsystem. To facilitate a comprehensive understanding, the equations governing the

Table 2
Exergy balance equations for each component in the envisaged trigeneration system.

Component	Exergy balance equations	Fuel exergy	Product exergy
MC	$\dot{E}_{10} + \dot{W}_{MC} = \dot{E}_{11} + \dot{E}_{d,MC}$	$\dot{W}_{MC}$	$\dot{E}_{10} - \dot{E}_{11}$
Reactor	$\dot{E}_1 + Q_R \cdot \left(1 - \frac{T_o}{T_R}\right) = \dot{E}_2 + \dot{E}_{d,R}$	$\dot{E}_1 + Q_R \cdot \left(1 - \frac{T_o}{T_R}\right)$	$\dot{E}_2$
RC	$\dot{E}_{5b} + \dot{W}_{RC} = \dot{E}_{12b} + \dot{E}_{d,RC}$	$\dot{W}_{RC}$	$\dot{E}_{12b} - \dot{E}_{5b}$
LTR	$\dot{E}_4 + \dot{E}_{11} = \dot{E}_5 + \dot{E}_{12a} + \dot{E}_{d,LTR}$	$\dot{E}_4 - \dot{E}_5$	$\dot{E}_{12a} - \dot{E}_{11}$
sCO_2 turbine	$\dot{E}_2 = \dot{E}_3 + \dot{W}_{TUR1} + \dot{E}_{d,TUR1}$	$\dot{E}_2 - \dot{E}_3$	$\dot{W}_{TUR1}$
HTR	$\dot{E}_3 + \dot{E}_{12} = \dot{E}_1 + \dot{E}_4 + \dot{E}_{d,HTR}$	$\dot{E}_3 - \dot{E}_4$	$\dot{E}_1 - \dot{E}_{12}$
Pre-cooler	$\dot{E}_9 + \dot{E}_{13} = \dot{E}_{10} + \dot{E}_{14} + \dot{E}_{d,PC}$	$\dot{E}_9 - \dot{E}_{10}$	$\dot{E}_{14} - \dot{E}_{13}$
V.G 1	$\dot{E}_{5a} + \dot{E}_{24} = \dot{E}_6 + \dot{E}_{15} + \dot{E}_{d,GEN1}$	$\dot{E}_{5a} - \dot{E}_6$	$\dot{E}_{15} - \dot{E}_{24}$
Separator	$\dot{E}_{15} = \dot{E}_{16} + \dot{E}_{18} + \dot{E}_{d,SEP}$	$\dot{E}_{15}$	$\dot{E}_{16} + \dot{E}_{18}$
H.EX 1	$\dot{E}_6 + \dot{E}_{50} = \dot{E}_7 + \dot{E}_{51} + \dot{E}_{d,HEX1}$	$\dot{E}_6 - \dot{E}_7$	$\dot{E}_{51} - \dot{E}_{50}$
H.EX 2	$\dot{E}_7 + \dot{E}_{31} = \dot{E}_8 + \dot{E}_{32} + \dot{E}_{d,HEX2}$	$\dot{E}_7 - \dot{E}_8$	$\dot{E}_{32} - \dot{E}_{31}$
H.EX 3	$\dot{E}_{18} + \dot{E}_{23} = \dot{E}_{19} + \dot{E}_{24} + \dot{E}_{d,HEX3}$	$\dot{E}_{18} - \dot{E}_{19}$	$\dot{E}_{24} - \dot{E}_{23}$
KC turbine	$\dot{E}_{16} = \dot{E}_{17} + \dot{W}_{TUR2} + \dot{E}_{d,TUR2}$	$\dot{E}_{16} - \dot{E}_{17}$	$\dot{W}_{TUR2}$
E.V1	$\dot{E}_{19} = \dot{E}_{20} + \dot{E}_{d,EV1}$	$\dot{E}_{19}$	$\dot{E}_{20}$
Mixer	$\dot{E}_{17} + \dot{E}_{20} = \dot{E}_{21} + \dot{E}_{d,MIX}$	$\dot{E}_{17} + \dot{E}_{20}$	$\dot{E}_{21}$
Pump1	$\dot{E}_{22} + \dot{W}_{PUMP1} = \dot{E}_{23} + \dot{E}_{d,PUMP1}$	$\dot{W}_{PUMP1}$	$\dot{E}_{23} - \dot{E}_{22}$
H.EX 4	$\dot{E}_{21} + \dot{E}_{28} = \dot{E}_{22} + \dot{E}_{25} + \dot{E}_{d,HEX4}$	$\dot{E}_{21} - \dot{E}_{22}$	$\dot{E}_{25} - \dot{E}_{28}$
ORC turbine	$\dot{E}_{25} = \dot{E}_{26} + \dot{W}_{TUR3} + \dot{E}_{d,TUR3}$	$\dot{E}_{25} - \dot{E}_{26}$	$\dot{W}_{TUR3}$
Pump2	$\dot{E}_{27} + \dot{W}_{PUMP2} = \dot{E}_{28} + \dot{E}_{d,PUMP2}$	$\dot{W}_{PUMP2}$	$\dot{E}_{28} - \dot{E}_{27}$
H.EX 5	$\dot{E}_{26} + \dot{E}_{30} = \dot{E}_{27} + \dot{E}_{31} + \dot{E}_{d,HEX5}$	$\dot{E}_{26} - \dot{E}_{27}$	$\dot{E}_{31} - \dot{E}_{30}$
Pump3	$\dot{E}_{29} + \dot{W}_{PUMP3} = \dot{E}_{30} + \dot{E}_{d,PUMP3}$	$\dot{W}_{PUMP3}$	$\dot{E}_{30} - \dot{E}_{29}$
LNG turbine	$\dot{E}_{32} = \dot{E}_{33} + \dot{W}_{TUR4} + \dot{E}_{d,TUR4}$	$\dot{E}_{32} - \dot{E}_{33}$	$\dot{W}_{TUR4}$
V.G 2	$\dot{E}_8 + \dot{E}_{36} = \dot{E}_9 + \dot{E}_{37} + \dot{E}_{40} + \dot{E}_{d,GEN2}$	$\dot{E}_8 - \dot{E}_9$	$\dot{E}_{37} + \dot{E}_{40} - \dot{E}_{36}$
Condenser	$\dot{E}_{40} + \dot{E}_{48} = \dot{E}_{41} + \dot{E}_{49} + \dot{E}_{d,COND}$	$\dot{E}_{40} - \dot{E}_{41}$	$\dot{E}_{49} - \dot{E}_{48}$
Evaporator	$\dot{E}_{42} + \dot{E}_{46} = \dot{E}_{43} + \dot{E}_{47} + \dot{E}_{d,EVAP}$	$\dot{E}_{42} - \dot{E}_{43}$	$\dot{E}_{47} - \dot{E}_{46}$
SHX	$\dot{E}_{35} + \dot{E}_{37} = \dot{E}_{36} + \dot{E}_{38} + \dot{E}_{d,SHX}$	$\dot{E}_{37} - \dot{E}_{38}$	$\dot{E}_{36} - \dot{E}_{35}$
Absorber	$\dot{E}_{39} + \dot{E}_{43} + \dot{E}_{44} = \dot{E}_{34} + \dot{E}_{45} + \dot{E}_{d,ABS}$	$\dot{E}_{39} + \dot{E}_{43} - \dot{E}_{34}$	$\dot{E}_{45} - \dot{E}_{44}$
Pump4	$\dot{E}_{34} + \dot{W}_{PUMP4} = \dot{E}_{35} + \dot{E}_{d,PUMP4}$	$\dot{W}_{PUMP4}$	$\dot{E}_{35} - \dot{E}_{34}$
E.V2	$\dot{E}_{38} = \dot{E}_{39} + \dot{E}_{d,EV2}$	$\dot{E}_{38}$	$\dot{E}_{39}$
E.V3	$\dot{E}_{41} = \dot{E}_{42} + \dot{E}_{d,EV3}$	$\dot{E}_{41}$	$\dot{E}_{42}$
PEME	$\dot{E}_{51} + \dot{W}_{PEME} = \dot{E}_{52} + \dot{E}_{53} + \dot{E}_{d,PEME}$	$\dot{E}_{51} + \dot{W}_{PEME}$	$\dot{E}_{52} + \dot{E}_{53}$

determination of chemical exergy, physical exergy, and overall exergy are thoughtfully presented below [34]:

$$\dot{E} = \dot{E}_{ph} + \dot{E}_{ch} \tag{4}$$

$$\dot{E}_{ph} = \dot{m}\left[(h - h_o) - T_o(s - s_o)\right] \tag{5}$$

$$\dot{E}_{ch} = \dot{m}\left[\left(\frac{X}{M_{NH_3}}\right) e^0_{ch,NH_3} + \left(\frac{1-X}{M_{H_2O}}\right) e^0_{ch,H_2O}\right] \tag{6}$$

In the previous equation, the terms e^0_{ch,NH_3} and e^0_{ch,H_2O} represent the standard chemical exergy values attributed to ammonia and water, respectively. These values are determined from the reference [34].

Electrolyzer model

Constructing a mathematical model for a PEME involves considering factors like hydrogen generation, power demands, and activation potentials. The potential difference between the electrodes drives water splitting, resulting in hydrogen and oxygen production. The anode, cathode, and overall reactions are as follows [35]:

$$\text{Anode}: \quad H_2O \rightarrow 2H^+ + 0.5O_2 + 2e^- \tag{7}$$

$$\text{Cathode}: \quad 2H^+ + 2e^- \rightarrow H_2 \tag{8}$$

$$\text{Overall}: \quad H_2O + energy \rightarrow H_2 + 0.5O_2 \tag{9}$$

The rate of hydrogen production ($\dot{m}_{H2}$) is calculated using Faraday's law of electrolysis, which establishes a direct relationship between the amount of substance generated at an electrode and the electric charge passing through it. This relationship is expressed by the following equation [35]:

$$\dot{m}_{H_2} = \frac{J}{2F} \tag{10}$$

In this context, the Faraday constant is denoted by F, and J signifies the electric current flowing through the electrochemical cell.

The electrical power consumed by the electrolyzer is determined by multiplying the electric current (J) by the applied voltage (V) [35].

$$\dot{W}_{PEME} = J \times V = \dot{W}_{KT} \tag{11}$$

It's important to highlight that in this study, the power generated by the KC is employed to drive the electrolyzer, and the voltage (V) of the electrolyzer is given by [35]:

$$V = V_o + V_{ohm} + V_{act,a} + V_{act,c} \tag{12}$$

V_o represents the thermodynamic potential of the hydrogen generation reaction and is defined as [35]:

$$V_0 = 1.229 - 8.5 \times 10^{-4}(T_{PEME} - 298) \tag{13}$$

The $V_{act,a}$ and $V_{act,c}$ signify the activation potential on the anode and cathode sides and can be expressed as follows [35]:

$$V_{act,i} = \frac{R \times T_{PEME}}{F} \sinh^{-1}\left(\frac{J}{2 \times J_{0,i}}\right), \quad i = a, c \tag{14}$$

The exchange current density of the electrolyzer, denoted as $J_{0,i}$, is determined as follows [35]:

$$J_{0,i} = J_i^{ref} \times \exp\left(-\frac{E_{act,i}}{R \times T_{PEME}}\right), \quad i = a, c \tag{15}$$

Additionally, the ohmic potential is defined as follows [35]:

$$V_{ohm} = J \times R_{PEME} \tag{16}$$

In this context, R_{PEME} represents the resistive losses attributed to the ionic conductivity of the electrolyte and the electrical resistance of the membrane. It can be mathematically expressed as [35]:

$$R_{PEME} = \int_0^L \frac{dx}{\sigma_{PEME}[\lambda(x)]} \tag{17}$$

σ_{PEME} [λ(x)] characterizes the ionic conductivity of the PEM electrolyte at position x, with λ(x) representing the water content at that location. The equations for calculating these parameters are provided in reference [35]:

$$\sigma_{PEME}[\lambda(x)] = [0.5139\lambda(x) - 0.326]\left[1268\left(\frac{1}{303} - \frac{1}{T_{PEME}}\right)\right] \tag{18}$$

Table 3
Equations for cost equilibrium and supporting parameters in the proposed trigeneration system components.

Component	Exergoeconomic cost balance equation	Supporting equation
MC	$\dot{C}_{11} = \dot{C}_{10} + \dot{C}_{W,MC} + \dot{Z}_{MC}$	$\dot{C}_{W,MC}/\dot{W}_{MC} = \dot{C}_{W,TUR1}/\dot{W}_{TUR1}$
Reactor	$\dot{C}_2 = \dot{C}_{fuel} + \dot{C}_1 + \dot{Z}_R$	nil
RC	$\dot{C}_{12b} = \dot{C}_{5b} + \dot{C}_{W,RC} + \dot{Z}_{RC}$	$\dot{C}_{5b} = SR \times \dot{C}_5, \dot{C}_{W,RC}/\dot{W}_{RC} = \dot{C}_{W,TUR1}/\dot{W}_{TUR1}$
LTR	$\dot{C}_5 + \dot{C}_{12a} = \dot{C}_4 + \dot{C}_{11} + \dot{Z}_{LTR}$	$\dot{C}_{12} = \dot{C}_{12a} + \dot{C}_{12b}, \dot{C}_4/\dot{E}_4 = \dot{C}_5/\dot{E}_5$
sCO_2 turbine	$\dot{C}_3 + \dot{C}_{W,TUR1} = \dot{C}_2 + \dot{Z}_{TUR1}$	$\dot{C}_2/\dot{E}_2 = \dot{C}_3/\dot{E}_3$
HTR	$\dot{C}_1 + \dot{C}_4 = \dot{C}_3 + \dot{C}_{12} + \dot{Z}_{HTR}$	$\dot{C}_3/\dot{E}_3 = \dot{C}_4/\dot{E}_4$
Pre-cooler	$\dot{C}_{10} + \dot{C}_{14} = \dot{C}_9 + \dot{C}_{13} + \dot{Z}_{PC}$	$\dot{C}_9/\dot{E}_9 = \dot{C}_{10}/\dot{E}_{10}, \dot{C}_{13} = 0$
V.G 1	$\dot{C}_6 + \dot{C}_{15} = \dot{C}_{5a} + \dot{C}_{24} + \dot{Z}_{GEN1}$	$\dot{C}_{5a}/\dot{E}_{5a} = \dot{C}_6/\dot{E}_6, \dot{C}_{5a} = (1 - SR) \times \dot{C}_5$
Separator	$\dot{C}_{16} + \dot{C}_{18} = \dot{C}_{15} + \dot{Z}_{SEP}$	$\dot{C}_{16}/\dot{E}_{16} = \dot{C}_{18}/\dot{E}_{18}, \dot{Z}_{SEP} = 0$
H.EX 1	$\dot{C}_7 + \dot{C}_{51} = \dot{C}_6 + \dot{C}_{50} + \dot{Z}_{HEX1}$	$\dot{C}_6/\dot{E}_6 = \dot{C}_7/\dot{E}_7, \dot{C}_{50} = 0$
H.EX 2	$\dot{C}_8 + \dot{C}_{32} = \dot{C}_7 + \dot{C}_{31} + \dot{Z}_{HEX2}$	$\dot{C}_7/\dot{E}_7 = \dot{C}_8/\dot{E}_8$
H.EX 3	$\dot{C}_{19} + \dot{C}_{24} = \dot{C}_{18} + \dot{C}_{23} + \dot{Z}_{HEX3}$	$\dot{C}_{18}/\dot{E}_{18} = \dot{C}_{19}/\dot{E}_{19}$
KC turbine	$\dot{C}_{17} + \dot{C}_{W,TUR2} = \dot{C}_{16} + \dot{Z}_{TUR2}$	$\dot{C}_{16}/\dot{E}_{16} = \dot{C}_{17}/\dot{E}_{17}$
E.V1	$\dot{C}_{20} = \dot{C}_{19} + \dot{Z}_{EV1}$	$\dot{Z}_{EV1} = 0$
Mixer	$\dot{C}_{21} = \dot{C}_{17} + \dot{C}_{20} + \dot{Z}_{MIX}$	$\dot{Z}_{MIX} = 0$
Pump1	$\dot{C}_{23} = \dot{C}_{22} + \dot{C}_{W,PUMP1} + \dot{Z}_{PUMP1}$	$\dot{C}_{W,PUMP1}/\dot{W}_{PUMP1} = \dot{C}_{W,TUR2}/\dot{W}_{TUR2}$
H.EX 4	$\dot{C}_{22} + \dot{C}_{25} = \dot{C}_{21} + \dot{C}_{28} + \dot{Z}_{HEX4}$	$\dot{C}_{21}/\dot{E}_{21} = \dot{C}_{22}/\dot{E}_{22}$
ORC turbine	$\dot{C}_{26} + \dot{C}_{W,TUR3} = \dot{C}_{25} + \dot{Z}_{TUR3}$	$\dot{C}_{25}/\dot{E}_{25} = \dot{C}_{26}/\dot{E}_{26}$
Pump2	$\dot{C}_{28} = \dot{C}_{27} + \dot{C}_{W,PUMP2} + \dot{Z}_{PUMP2}$	$\dot{C}_{W,PUMP2}/\dot{W}_{PUMP2} = \dot{C}_{W,TUR3}/\dot{W}_{TUR3}$
H.EX 5	$\dot{C}_{27} + \dot{C}_{31} = \dot{C}_{26} + \dot{C}_{30} + \dot{Z}_{HEX5}$	$\dot{C}_{26}/\dot{E}_{26} = \dot{C}_{27}/\dot{E}_{27}$
Pump3	$\dot{C}_{30} = \dot{C}_{29} + \dot{C}_{W,PUMP3} + \dot{Z}_{PUMP3}$	$\dot{C}_{W,PUMP3}/\dot{W}_{PUMP3} = \dot{C}_{W,TUR4}/\dot{W}_{TUR4}$
LNG turbine	$\dot{C}_{33} + \dot{C}_{W,TUR4} = \dot{C}_{32} + \dot{Z}_{TUR4}$	$\dot{C}_{32}/\dot{E}_{32} = \dot{C}_{33}/\dot{E}_{33}$
V.G 2	$\dot{C}_9 + \dot{C}_{37} + \dot{C}_{40} = \dot{C}_8 + \dot{C}_{36} + \dot{Z}_{GEN2}$	$\left(\dot{C}_{40} - \dot{C}_{36}\right) \Big/ \left(\dot{E}_{40} - \dot{E}_{36}\right) = \left(\dot{C}_{37} - \dot{C}_{36}\right) \Big/ \left(\dot{E}_{37} - \dot{E}_{36}\right) \dot{C}_8/\dot{E}_8 = \dot{C}_9/\dot{E}_9$
Condenser	$\dot{C}_{41} + \dot{C}_{49} = \dot{C}_{40} + \dot{C}_{48} + \dot{Z}_{COND}$	$\dot{C}_{40}/\dot{E}_{40} = \dot{C}_{41}/\dot{E}_{41}, \dot{C}_{48} = 0$
Evaporator	$\dot{C}_{43} + \dot{C}_{47} = \dot{C}_{42} + \dot{C}_{46} + \dot{Z}_{EVAP}$	$\dot{C}_{42}/\dot{E}_{42} = \dot{C}_{43}/\dot{E}_{43}, \dot{C}_{46}/\dot{E}_{46} = \dot{C}_{47}/\dot{E}_{47}$
SHX	$\dot{C}_{36} + \dot{C}_{38} = \dot{C}_{35} + \dot{C}_{37} + \dot{Z}_{SHX}$	$\dot{C}_{37}/\dot{E}_{37} = \dot{C}_{38}/\dot{E}_{38}$
Absorber	$\dot{C}_{28} + \dot{C}_{37} = \dot{C}_{27} + \dot{C}_{33} + \dot{C}_{36} + \dot{Z}_{ABS}$	$\dot{C}_{34}/\dot{E}_{34} = \left(\dot{C}_{39} + \dot{C}_{43}\right) \Big/ \left(\dot{E}_{39} + \dot{E}_{43}\right), \dot{C}_{44} = 0$
Pump4	$\dot{C}_{35} = \dot{C}_{34} + \dot{C}_{W,PUMP4} + \dot{Z}_{PUMP4}$	$\dot{C}_{W,PUMP4}/\dot{W}_{PUMP4} = \dot{C}_{W,TUR2}/\dot{W}_{TUR2}$
E.V2	$\dot{C}_{39} = \dot{C}_{38} + \dot{Z}_{EV2}$	$\dot{Z}_{EV2} = 0$
E.V3	$\dot{C}_{42} = \dot{C}_{41} + \dot{Z}_{EV3}$	$\dot{Z}_{EV3} = 0$
PEME	$\dot{C}_{52} + \dot{C}_{53} = \dot{C}_{51} + \dot{C}_{W,PEME} + \dot{Z}_{PEME}$	$\dot{C}_{W,PEME}/\dot{W}_{PEME} = \dot{C}_{W,TUR2}/\dot{W}_{TUR2}, \left(\dot{C}_{52} - \dot{C}_{51}\right) \Big/ \left(\dot{E}_{52} - \dot{E}_{51}\right) = \left(\dot{C}_{53} - \dot{C}_{51}\right) \Big/ \left(\dot{E}_{53} - \dot{E}_{51}\right)$

$$\lambda(x) = \frac{\lambda_a - \lambda_c}{D} x + \lambda_c \tag{19}$$

Exergoeconomic assessment

Exergoeconomic analysis is a widely recognized method utilized in engineering and energy systems, offers a comprehensive assessment that simultaneously evaluates economic and thermodynamic performance. This method seamlessly merges exergy analysis, which scrutinizes energy quality and losses, with economic analysis, which delves into resource and component expenses. By scrutinizing both exergy destruction and costs, this approach unveils inefficiencies and appraises the economic viability of system components [34]. It plays a pivotal role in pinpointing areas for enhancement, optimizing design, and judiciously allocating resources. While investing additional capital can enhance the thermodynamic performance of energy conversion systems, achieving an equilibrium between capital costs and efficiency improvements remains of paramount importance. In this section, exergoeconomic models are introduced to assess the performance of the proposed trigeneration system. This involves calculating its cost per unit of exergy, providing a comprehensive evaluation of both its economic and thermodynamic performance [36].

$$\sum \dot{C}_{out,k} + \dot{C}_{w,k} = \sum \dot{C}_{in,k} + \dot{C}_{q,k} + \dot{Z}_k \tag{20}$$

where,

$$\dot{C} = c\dot{E} \tag{21}$$

In this equation, "c" represents the cost of each unit of exergy stream [37].

The cost rate for the kth component, symbolized as ($\dot{Z}_k$) in Equation (21), encompasses the yearly capital investment rate ($\dot{Z}_k^{CI}$), and the yearly maintenance and operational cost rate ($\dot{Z}_k^{OM}$), as stated in [37]:

$$\dot{Z}_k = \dot{Z}_k^{CI} + \dot{Z}_k^{OM} \tag{22}$$

The capital investment rate for the k_{th} component can be expressed as [37]:

$$\dot{Z}_k^{CI} = \left(\frac{CRF}{\tau}\right) Z_k \tag{23}$$

The Capital Recovery Factor (CRF) is a vital parameter for evaluating the influence of the interest rate. In this particular study, τ denotes the total annual hours of operation, which has been set at 8,000 h [37]. The CRF is mathematically defined as follows:

$$CRF = \frac{i_r(1 + i_r)^n}{(1 + i_r)^n - 1} \tag{24}$$

The provided equation incorporates a 12 % interest rate applied over a

Table 4
Comparison between the present findings and those reported in Ref. [38] for the SCRBC cycle.

Parameter	Reference [38]	Current work	Error (%)
Net power generation (kW)	248.84	248.9	0.03
Energy performance (%)	41.46	41.483	0.029
Exergy performance (%)	57.47	57.528	0.087

Table 5
Comparison between the present findings and those reported in Ref. [39] for the KC cycle.

Parameter	Reference [39]	Current work	Error (%)
KC turbine input pressure	3000 kPa	3000 kPa	–
KC turbine exit pressure	926 kPa	926 kPa	–
KC turbine input temperature	151.4 °C	151.4 °C	–
Mass fraction of ammonia	0.6	0.6	–
Energy efficiency	6.94 %	7.05 %	1.46 %

Table 6
Comparison between the present findings and those reported in Ref. [40] for the ORC cycle.

Parameter	Reference [40]	Present work	Error (%)
Working fluid	Isopentane	Isopentane	–
Minimum temperature (°C)	29	29	–
Maximum temperature (°C)	110.4	110.4	–
Maximum pressure (bar)	8.98	8.98	–
Mass flow rate (kg/s)	80.13	80.37	0.3
Net work output (kW)	5270	5293	0.43
Thermal efficiency (%)	14.1	14.13	0.21

Table 7
Comparison between the present findings and those reported in Ref. [41] for the ARC cycle.

State points	T (°C)			$\dot{m}$(kg/s)		
	Current work	Ref. [41]	Error (%)	Current work	Ref. [41]	Error (%)
34	33.14	33.14	–	0.057	0.057	–
35	33.146	33.15	0.012	0.057	0.057	–
36	59.18	59.25	0.118	0.057	0.057	–
37	81.39	81.39	–	0.05181	0.0519	0.173
38	50.51	50.51	–	0.05181	0.0519	0.173
39	50.51	50.51	–	0.05181	0.0519	0.173
40	81.39	81.39	–	0.00519	0.0051	1.76
41	38.22	38.4	0.47	0.00519	0.0051	1.76
42	5.67	5.67	–	0.00519	0.0051	1.76
43	5.67	5.67	–	0.00519	0.0051	1.76

20-year duration, with the objective of assessing its impact on capital investments.

The cost rate associated with the maintenance and operation of the k^{th} component can be expressed as [38]:

$$\dot{Z}_k^{OM} = \gamma Z_k / \tau \tag{25}$$

In terms of the maintenance and operational costs, a weighting coefficient of 0.1 is employed [37].

In this investigation, we embark on the development of a comprehensive set of cost balance equations and auxiliary equations pertaining to the components within our proposed trigeneration system. Leveraging the capabilities of EES software, we gain the capacity to precisely compute the cost rates associated with a range of exergy streams. These equations are meticulously detailed and can be found in Table 3. Complete information regarding the cost functions (Z_k) for evaluating the expenses associated with all components of the proposed system during the thermoeconomic analysis is available in the Appendix.

Performance evaluation metrics

In this research, a thorough evaluation is carried out to examine the thermodynamic and financial aspects of the suggested trigeneration system using a variety of performance indicators. Assessing the system's efficiency is a critical objective, and, therefore, we consider several key metrics, specifically energy efficiency (η_{en}), exergy efficiency (η_{ex}), and overall cost of the product ($c_{P,total}$). These criteria are defined by the following expressions, which will serve as the basis for our analysis [25]:

$$\eta_{en} = \frac{\dot{W}_{net} + \dot{Q}_{EVAP} + \dot{m}_{H_2} LHV_{H_2}}{\dot{Q}_R} \tag{26}$$

where, W_{net} is the net power output, Q_{EVAP} stands for the cooling load, and m_{H2} is the hydrogen production rate, which can be expressed as:

$$\dot{W}_{net} = \dot{W}_{TUR1} + \dot{W}_{TUR2} + \dot{W}_{TUR3} + \dot{W}_{TUR4} - \dot{W}_{MC} - \dot{W}_{RC} - \dot{W}_{Pump1} - \dot{W}_{Pump2} - \dot{W}_{Pump3} - \dot{W}_{Pump4} - \dot{W}_{PEME} \tag{27}$$

The second law of thermodynamics plays a fundamental role in evaluating the performance of a system, especially in the context of exergy efficiency. The mathematical representation of the exergy supplied to the trigeneration system is as follows [34]:

$$\dot{E}_R = \dot{Q}_R \left(1 - \frac{T_o}{T_R}\right) \tag{28}$$

The exergetic efficiency of the trigeneration system can be defined as follows [34]:

$$\eta_{ex} = \frac{\dot{W}_{net} + \dot{Q}_{EVAP}\left(1 - \frac{T_o}{T_{42}}\right) + \dot{E}_{52}}{\dot{E}_R + \left(\dot{E}_{29} - \dot{E}_{33}\right)} \tag{29}$$

The total product unit cost can be defined as [34]:

$$c_{P,tot} = \frac{\dot{C}_{w,net} + \dot{C}_{47} + \dot{C}_{52}}{\dot{W}_{net} + \dot{E}_{47} + \dot{E}_{52}} \tag{30}$$

Validation of the models

The proposed trigeneration system integrates several key subsystems, including the SCRBC, KC, ORC, LiBR-H_2O ARC, and a PEME. For our research to maintain its reliability and applicability, it is crucial to verify the accuracy of the theoretical analyses employed for evaluating the efficiency of individual subsystems in the suggested trigeneration system. Our validation efforts commence with an examination of the SCRBC system, where we compare our results with previously published data, as summarized in Table 4 [38]. Additionally, for the KC subsystem, we compare our findings with data from the work of Hettiarachchi et al. [39], which includes various generator pressures, as detailed in Table 5. Furthermore, for the ORC cycle, we present a comparison between our study's results and those of Chacartegui's research [40], as showcased in Table 6. Moreover, we validate the LiBR-H_2O ARC by juxtaposing our results with data from existing literature, as illustrated in Table 7 [41]. The high precision of the validation process is confirmed by comparing the calculated thermodynamic parameters listed in Tables 4–7 with the findings of other researchers. Additionally, in Fig. 2, we provide visual representation of the PEME validation, revealing a high degree of accuracy in voltage output when compared to

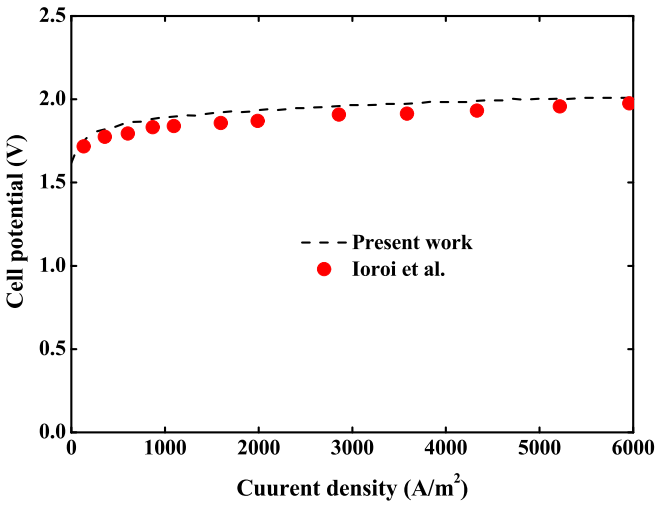


Fig. 2. Validation of Electrolyzer Model Using Ioroi et al.'s Work [42].

Table 8
Essential input variables for thermodynamic analysis.

Variable	Value	Variable	Value
T_o (°C)	25	T_{50} (°C)	25
P_o (kPa)	101.3	T_{50} (°C)	80
P_{10} (kPa)	7400	$T_{19} - T_{23}$ (°C)	10
P_{VG1} (kPa)	3000	$TTD_{,VG1}$ (°C)	10
PRc	3	$\Delta T_{PPT,VG1}$ (°C)	10
T_{10} (°C)	35	$\Delta T_{VG2,hot}$ (°C)	10
T_2 (°C)	550	$\Delta T_{VG2,cold}$ (°C)	3
T_R (°C)	800	η_{MC}&η_{RC}	0.85
T_{42} (°C)	8	η_{T1}&η_{T2}&η_{T3}&η_{T4}	0.9
T_{44} (°C)	25	H_{Pum1}&η_{Pum2}&η_{Pum3}&η_{Pum4}	0.85
T_{45} (°C)	30	ϵ_{HTR} & ϵ_{LTR}	0.86
T_{46} (°C)	15	ϵ_{SHX}	0.82
T_{47} (°C)	10	X_{15} (%)	50
T_{48} (°C)	25	$\Delta T_{PPT,HEX1,4}$ (°C)	10
T_{49} (°C)	30	$TTD_{,HEX2}$ (°C)	20
T_{13} (°C)	25	NG turbine P_{in} (kPa)	3000
T_{14} (°C)	50	NG turbine P_{out} (kPa)	450
Q_R (MW)	600	LNG tank temperature (°C)	−161.5
ORC condensation temperature (°C)	−35	LNG tank pressure (kPa)	101.3
T_{34} (°C)	33	Quality of methane at state 31	1

Table 9
Comparative analysis of the conventional SCRBC system and the proposed trigeneration system in the base design scenario.

Performance parameters	SCRBC system	Proposed trigeneration system
Net power output of the cycle ($\dot{W}_{net}$)	237.89 MW	276.706 MW
Cooling output (Q_{EVAP})	–	60.193 MW
Hydrogen production (m_{H2})	–	176.25 kg/hr
Energy efficiency (η_{en})	39.6 (%)	57.8 (%)
Exergy efficiency(η_{ex})	54.38 (%)	59.46 (%)
Cost per unit of the system's product ($c_{P;tot}$)	12.27 ($/GJ)	11.642 ($/GJ)

the findings of Ioroi et al. [42].

Results and discussion

This section provides an overview of the research findings, which primarily focus on the energy, exergy, and exergoeconomic performance of the trigeneration system. Our study employs a parametric analysis to systematically assess the impact of different variables on the system's thermodynamics and exergoeconomics. The obtained insights serve as a guiding framework for optimizing parameters through GA optimization technique. Lastly, we conduct a comprehensive comparative evaluation, highlighting the distinct advantages of the proposed trigeneration system against those of the traditional SCRBC system.

Evaluation of thermodynamic and exergoeconomic performance

For a comprehensive evaluation of the efficiency of the recently introduced trigeneration system, an exhaustive analysis was carried out using EES software. Table 8 succinctly encapsulates the input parameters utilized in this study. Additionally, thermodynamic characteristics and exergy stream costs for each component in the proposed trigeneration system are detailed in Table A3 in the Appendix.

Table 9 offers a comprehensive comparative analysis, pitting the conventional SCRBC system against the innovative trigeneration system. This evaluation employs a multi-pronged approach, encompassing energy, exergy, and product cost considerations. Separately, the SCRBC cycle, focused solely on power generation, yields a commendable net output of 237.89 MW. However, the trigeneration system takes the lead with an impressive production of 274.976 MW, representing a remarkable 15.6 % boost in net power output. Moreover, the proposed trigeneration system demonstrates its versatility by efficiently delivering a cooling load of 60.193 MW. It's worth noting that the entirety of the net power output generated by the KC is dedicated to powering the PEME for hydrogen production, yielding an impressive mass flow rate of approximately 176.25 kg/hr. When we consider energy and exergy efficiency, the contrast becomes even more evident. While the standalone SCRBC system boasts energy and exergy efficiencies of 39.6 % and 54.38 %, respectively, the proposed system excels with energy and exergy efficiencies of 54.38 % and 59.46 %, signifying substantial improvements of 37.3 % and 9.34 %, respectively. Additionally, the introduction of the trigeneration system also ushers in a remarkable reduction in the total product unit cost of the SCRBC system. The cost per unit drops from $12.272/GJ to a more economical $11.642/GJ, marking a significant 5.41 % cost reduction. However, it's important to underline that these results are grounded in base design conditions, leaving room for further enhancements in energy, exergy, and cost performance through the application of optimization techniques. These possibilities will be explored in greater detail in subsequent discussions.

Parametric study

In this section, we delve into a comprehensive parameter analysis of the proposed trigeneration system. Parameter analysis is a pivotal step in our research, offering valuable insights into how key variables influence system design performance. This analysis serves as a crucial foundation for subsequent parameter optimization efforts. Our focus is on assessing the impact of key variables on the overarching performance metrics, including energy efficiency (η_{en}), exergy efficiency (η_{ex}), and the unit cost of product output ($c_{p,total}$). The variables under scrutiny encompass a range of critical factors, including the sCO_2 compressor pressure ratio (PRc), sCO_2 turbine inlet temperature (T_2), VG1 pressure of the KC (P_{VG1}), terminal temperature difference of VG1 (TTD_{VG1}), ammonia-water concentration (X_{15}), hot end temperature difference of VG2 ($\Delta T_{VG2,hot}$), and the evaporation temperature (T_{eva}). In our parametric analysis, we adopt a rigorous approach by keeping all other parameters constant, as specified in Table 8, when investigating the effect of a single parameter. This meticulous examination allows us to gain a deeper understanding of how each variable impacts the system's overall performance, facilitating informed decisions for optimization strategies.

Influence of compressor pressure ratio (PR_C)

Fig. 3 (a, b) illustrates the impact of PR_C on the performance of the proposed trigeneration system. Emphasizing the significance of PR_C is crucial because it determines the peak cycle pressure and exerts a

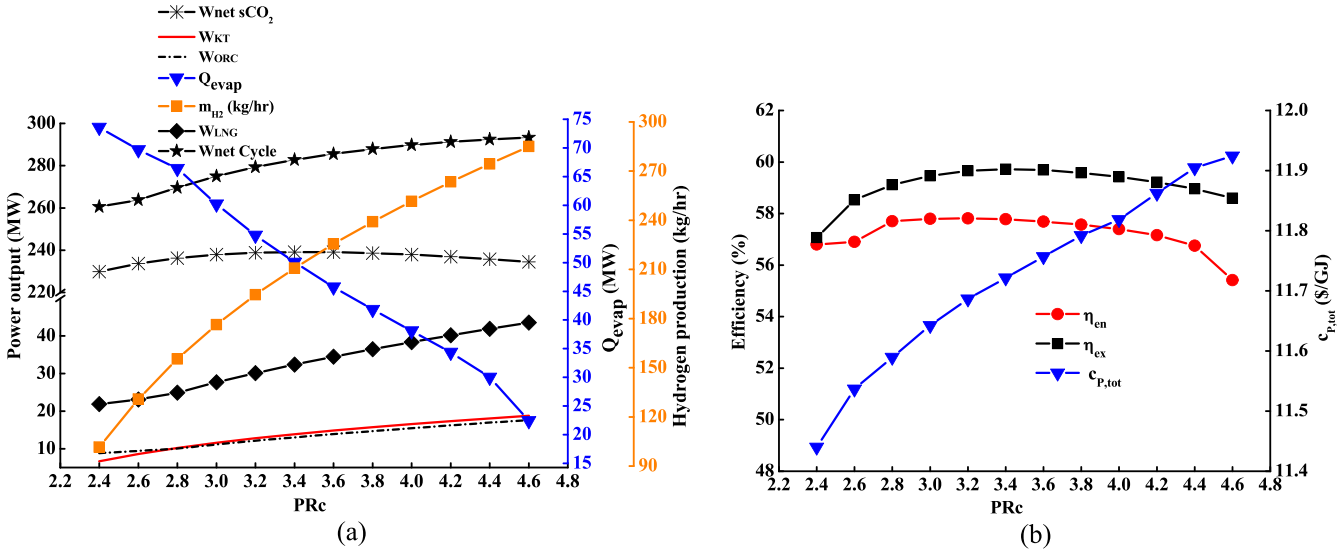


Fig. 3. Impacts of PRc on: (a) $W_{net,sCO2}$,W_{KT}, W_{ORC}, W_{LNG}, $W_{net,Cycle}$, Q_{evap}, and m_{H2}, and (b) η_{en}, η_{ex} & $c_{p,tot}$.

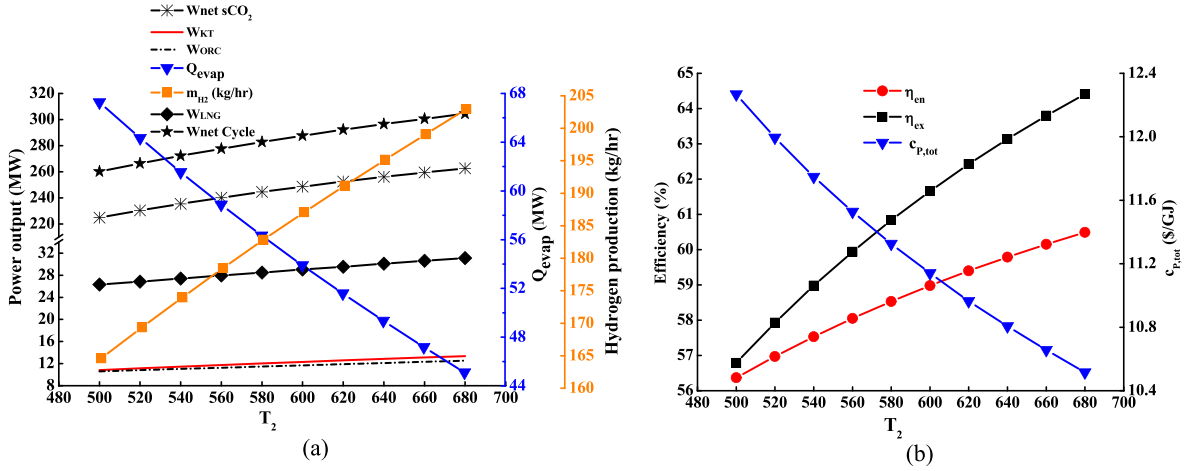


Fig. 4. Impacts of T_2 on: (a) $W_{net,sCO2}$,W_{KT}, W_{ORC}, W_{LNG}, $W_{net,Cycle}$, Q_{evap}, and m_{H2}, and (b) η_{en}, η_{ex} & $c_{p,tot}$.

substantial influence on the topping SCRBC subsystem's performance. As a result, the variations in the overall system's performance as PR_C increases primarily result from the behaviour of the topping SCRBC subsystem. In Fig. 3(a), it is visually evident that the electrical power generated by the upper SCRBC subsystem initially increases with an escalating PR_C until it reaches an optimal PR_C, resulting in the maximum output. Beyond this point, the net power output begins to decline. This observed pattern arises from the interplay between higher compressor power consumption and increased turbine power production at elevated PR_C values, ultimately defining the optimal pressure ratio (at PRc = 3.4) that yields the maximum electrical power output.

With an elevated PR_C, several notable changes transpire. Initially, there is a discernible decrease in the mass flow rate of the CO_2 stream, primarily attributed to the fixed turbine inlet temperature, causing lower turbine outlet temperatures with the rising PR_C. Consequently, there is a decline in the temperature at the cold outlet of the HTR, inducing a more substantial temperature upswing in the CO_2 stream passing through the reactor while maintaining constant heat input. The reduction in the mass flow rate of the CO_2 stream within the topping sCO_2 system corresponds to a decrease in the heat flux of the generator. However, counteracting effects emerge. The increased PR_C results in higher compressor outlet temperatures, subsequently elevating the temperatures at the hot outlets of both the LTR and HTR. This enhancement contributes to an elevated temperature at which the CO_2 stream enters the generator, leading to an increased heat flux within the generator. It is noteworthy that the impact of the rising temperature of the hot fluid on the generator's thermal flux has a more pronounced effect than the decrease in the mass flow rate of the hot fluid considered in this analysis. Consequently, there is a more efficient recovery of waste heat within the generator. As a result, the flow rate of saturated vapor mass leaving the separator increases, accompanied by a simultaneous rise in the enthalpy drop across the KC turbine. These alterations culminate in a corresponding upturn in the power output of the KC turbine, as illustrated in Fig. 3(a).

Elevating the PR_C triggers several notable effects within the system. Initially, it diminishes the CO_2 flow rate through VG1, leading to a reduction in the mass flow rate of NH_3-H_2O solution within the KC. This decrease influences the heat flux in HEX4, a critical heat source for the ORC cycle. However, as the PR_C increases, the separator temperature rises, leading to a corresponding increase in the temperature of the NH_3-H_2O stream entering HEX4. This substantial temperature boost significantly augments the heat flux in HEX4, offsetting the impact of the reduced NH_3-H_2O mass flow rate. Consequently, this results in heightened waste heat recovery and an increased power output from the ORC turbine. The enhanced heat flux in HEX4, in turn, amplifies the mass flow rate of Isobutane within the ORC cycle. This augmentation elevates

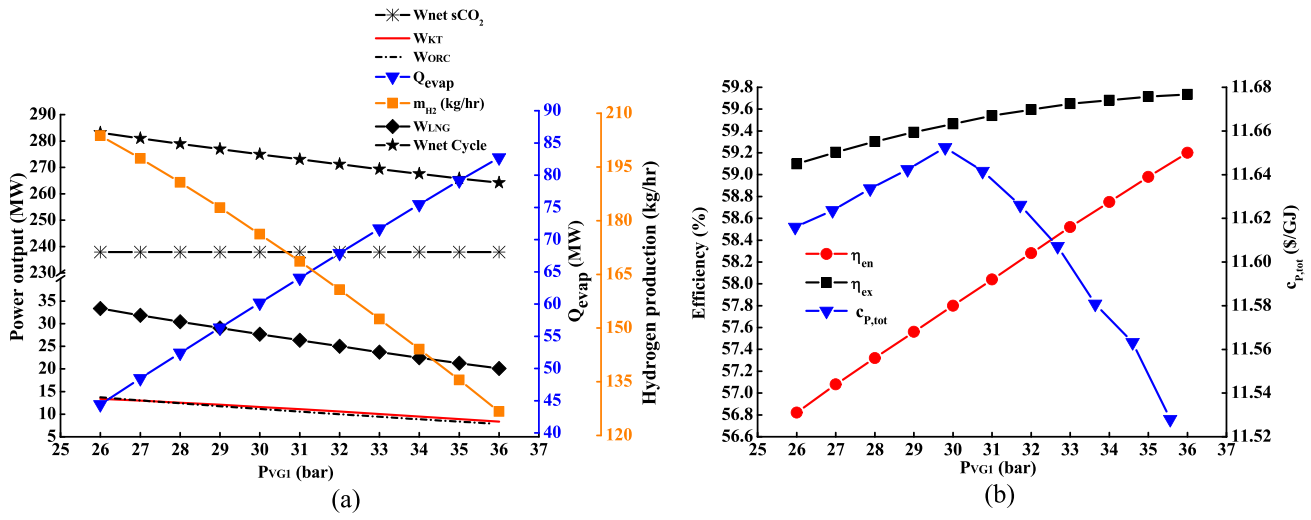


Fig. 5. Impacts of P_{VG1} on: (a) $W_{net,sCO2}$,W_{KT}, W_{ORC}, W_{LNG}, $W_{net,Cycle}$, Q_{evap}, and m_{H2}, and (b) η_{en}, η_{ex} & $c_{p,tot}$.

the heat flux in HEX5, subsequently boosting the power output of the NG turbine, as depicted in Fig. 3(a). These results contribute to a linear growth in the overall power output of the trigeneration system, as depicted in Fig. 3(a). Additionally, it's noteworthy that a higher corresponds with a decrease in cooling load due to reduced CO_2 flow through VG2. This PR_C reduction affects the heat flux in VG2 and the refrigerant flow through the evaporator, ultimately resulting in a decreased cooling load. Moreover, it is crucial to emphasize the direct correlation between hydrogen production (m_{H2}) and the electricity generation from the KC. As illustrated in Fig. 3(a), m_{H2} exhibits a steady linear growth as the PR_C increases, reflecting the observed pattern in KC power generation compared to PR_C.

Fig. 3(b) presents the relationships between energy efficiency (η_{en}), exergy efficiency (η_{ex}), and unit cost of product output ($c_{p,total}$) for the proposed trigeneration system across different PR_C values. It can be observed from Fig. 3(b) that the η_{en} and η_{ex} of the trigeneration system initially increase and then decrease in response to changes in the PR_C, which corresponds to the variation pattern of the total electrical power output of the SCRBC subsystem. Conversely, the $c_{p,total}$ exhibits a linear increase with changing PR_C values.

Influence of temperature at the turbine inlet (T_2)

Fig. 4 (a,b) illustrates how T_2 affects the performance of the proposed trigeneration system. Highlighting the significance of T_2 is essential since it establishes the peak cycle temperature for the entire system and exerts a substantial influence on the overall system performance. It is apparent that boosting the T_2 can effectively increase the electrical power generated by the sCO_2 turbine. Nevertheless, a possible consequence of such an increase is a decrease in the mass flow rate of the working fluid through the turbine and compressors. This reduction, in turn, leads to a decline in the compressor energy consumption and an overall improvement of the net topping cycle power output ($W_{net,\ sCO2}$), as evidenced in Fig. 4 (a).

Fig. 4(a) also illustrates the power output variation for the bottoming KC system. It's evident that the power generated by the KC system rises linearly with an elevation in T_2. As previously discussed, the consequence of increasing T_2 is a reduction in the sCO_2 stream flowing through VG1, subsequently lowering the NH_3-H_2O stream flow in the KC system (m_{15}). However, the increase in T_2 results in a higher separator temperature, which positively impacts the mass of saturated vapor (m_{16}) leaving the separator toward the KT, and it also increases the enthalpy difference across the KT. Both of these factors contribute to an improvement in the KT's power output. Additionally, as T_2 increases, Fig. 4(a) indicates that despite a decrease in the mass flow rate of the NH_3-H_2O stream passing through HEX4, the power output of the ORC system increases. This is because the enthalpy of the NH_3-H_2O stream entering HEX4 rises with increasing T_2, offsetting the decline in the NH_3-H_2O mass flow rate. Consequently, there is an increase in heat recovery from the NH_3-H_2O stream in HEX4, leading to an enhanced power output of the ORC system. This increase in ORC power output positively affects the power output of the NG turbine, resulting in a linear rise in the overall system's net power output as T_2 increases, as depicted in Fig. 4(a).

Furthermore, it is important to highlight that an increase in T_2 is linked to a reduction in the cooling load. This decline is attributed to the diminished flow of CO_2 through VG2, influencing the heat flux in VG2 and the flow of refrigerant through the evaporator. As a result, the cooling load experiences a decrease. Moreover, it is essential to underscore the direct relationship between hydrogen production (m_{H2}) and the power generation of KC. As depicted in Fig. 4(a), m_{H2} demonstrates a steady linear growth with higher T_2.

Fig. 4 (b) demonstrates the variation in the parameters η_{en}, η_{ex}, and $c_{p,total}$ with respect to T_2 in the proposed trigeneration system. It is evident that the η_{en} and η_{ex} increase proportionally as T_2 rises, while $c_{p,\ total}$ decreases linearly. Moreover, the η_{en} shows a slower increment rate compared to η_{ex}. As the cooling load decreases at a substantially slower rate than the net output power increment, the proposed trigeneration system exhibits improved η_{en} and η_{ex} with increasing T_2. Additionally, the total investment in the trigeneration system decreases as the working fluid mass flow rate decreases. The increase in electrical power output and the decrease in the total investment of system components assist in the reduction in the overall unit cost of the product. Therefore, an elevation in T_2 leads to a reduction in the overall product unit cost.

Influence of KC vapor generator 1 pressure (P_{VG1})

The impact of P_{VG1} on the performance metrics of the proposed trigeneration system is displayed in Fig. 5 (a,b). Increasing the pressure of the NH_3-H_2O solution in the generator, while keeping the temperature constant, presents challenges in separating the saturated vapor stream from the solution. As a result, higher P_{VG1} leads to a decrease in the flow rate of vapor in its saturated state. This means that although higher pressure vapor can produce greater power per flow rate unit, the poorer mass flow rate through the turbines counterbalances this advantage and decreases power output. Therefore, as P_{VG1} increases, the overall electrical power production of the KC system decreases. This happens primarily because the decrease in vapor mass flow rate has a stronger impact on power output compared to the effect of the increasing expansion ratio. This is illustrated in Fig. 5 (a).

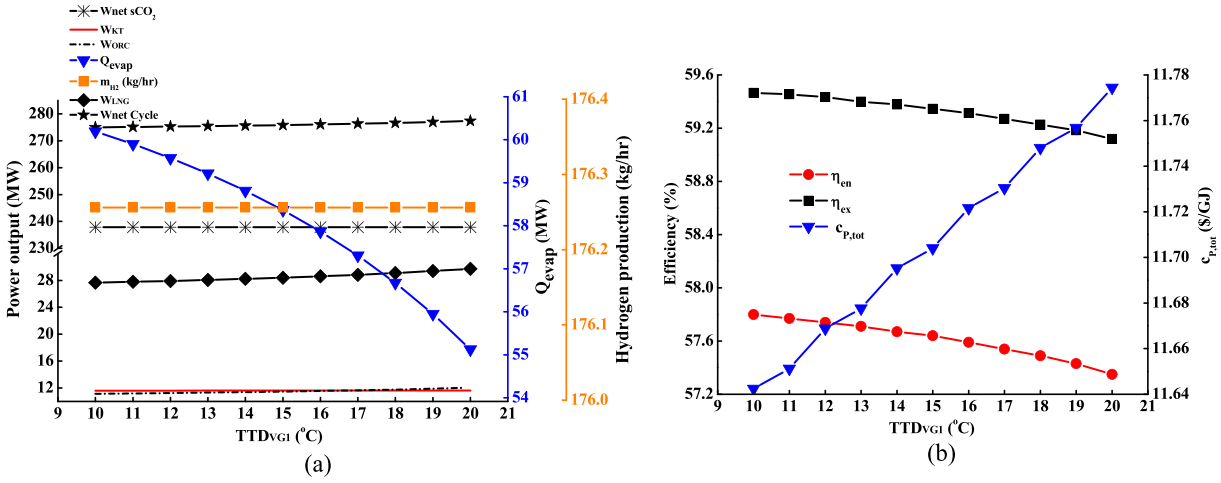


Fig. 6. Impacts of TTD_{VG1} on: (a) $W_{net,sCO2}$,W_{KT}, W_{ORC}, W_{LNG}, $W_{net,Cycle}$, Q_{evap}, and m_{H2}, and (b) η_{en}, η_{ex} & $c_{p,tot}$.

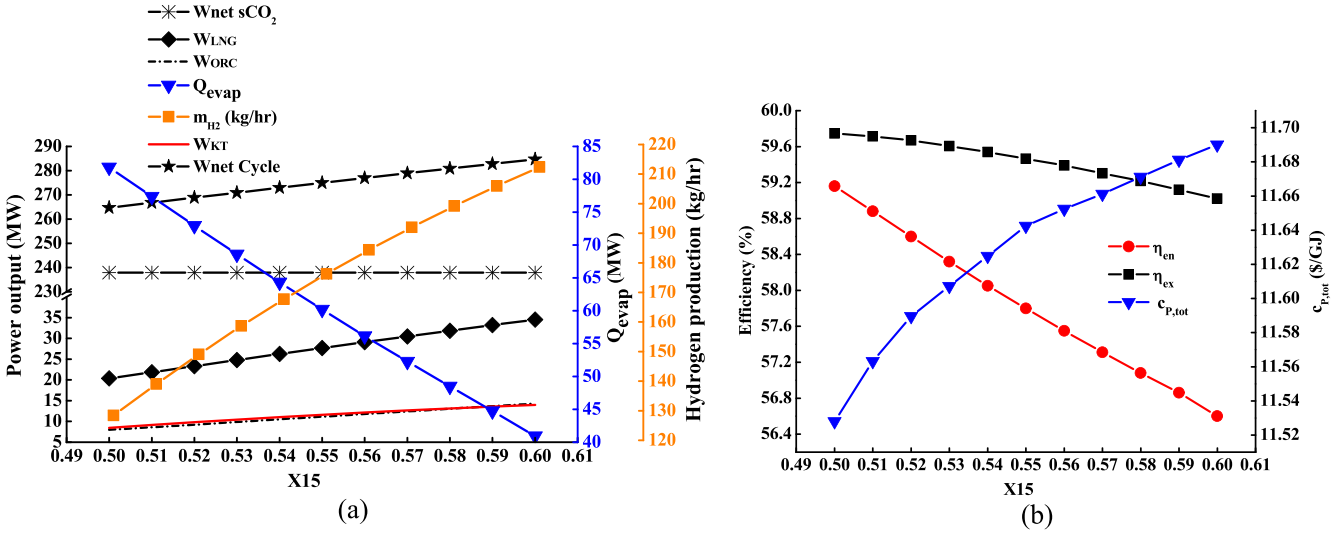


Fig. 7. Impacts of X_{15} on: (a) $W_{net,sCO2}$,W_{KT}, W_{ORC}, W_{LNG}, $W_{net,Cycle}$, Q_{evap}, and m_{H2}, and (b) η_{en}, η_{ex} & $c_{p,tot}$.

On the contrary, when P_{VG1} is elevated, the results depicted in Fig. 5 (a) unveil an intriguing pattern. Despite the increase in the mass flow rate of the NH_3-H_2O stream passing through HEX4, there is a reduction in the power output of the ORC. This counterintuitive effect arises from the fact that as P_{VG1} increases, the enthalpy of the NH_3-H_2O stream entering HEX4 decreases, offsetting the rise in NH_3-H_2O mass flow rate. Consequently, there is a decrease in the heat recovery from the NH_3-H_2O stream in HEX4, leading to a diminished power output in the ORC system. This decline in ORC power output, in turn, adversely affects the power output of the NG turbine, resulting in a linear decrease in the overall system's net power output as P_{VG1} increases, as depicted in Fig. 5 (a).

Furthermore, it's worth highlighting that a higher P_{VG1} corresponds to an increased cooling load. This rise can be attributed to the elevated temperature of the CO_2 stream exiting VG1, which, in turn, raises the enthalpy of the CO_2 stream entering VG2 in the ARC cycle. This increase in enthalpy amplifies the heat flux in VG2 and the mass flow of refrigerant through the evaporator, resulting in an overall increase in the cooling load. Additionally, it's crucial to underscore the direct relationship between hydrogen production (m_{H2}) and the power generation of KC. As demonstrated in Fig. 5 (a), m_{H2} consistently exhibits a linear decrease as P_{VG1} rises.

The data presented in Fig. 5 (b) illustrates a notable trend: an increase in P_{VG1} corresponds to a linear rise in the energy efficiency of the system. This phenomenon is driven by the fact that the rise in cooling capacity outweighs the decrease in the overall electrical power output, leading to a continuous improvement of energy efficiency. Moreover, Fig. 5 (b) also demonstrates an interesting observation: while the decline in the overall electrical power output of the system surpasses the increase in cooling exergy, the exergy efficiency follows an upward trajectory. This intriguing observation can be attributed to the reduction in exergy input to the LNG stream due to a significant decrease in the amount of heat recovered in HEX5, thereby leading to an increase in exergy efficiency. Furthermore, it becomes evident that as P_{VG1} increases, $c_{p,total}$ initially rises until it reaches a peak value, after which it starts to decline. This pattern indicates that at high P_{VG1} levels, the system reveals favorable economic characteristics.

Influence of terminal temperature difference of VG1 (TTD_{VG1})

Fig. 6 (a,b) provides a detailed depiction of how the TTD_{VG1} impacts various output performance parameters within the proposed trigeneration system. TTD_{VG1}, defined as the difference between the exit temperature of LTR (T_5) and the separator temperature, plays a central role in shaping these outcomes. As TTD_{VG1} experiences an increase, it triggers a simultaneous decrease in the separator temperature, with T_5 remaining consistently maintained. This reduction in separator

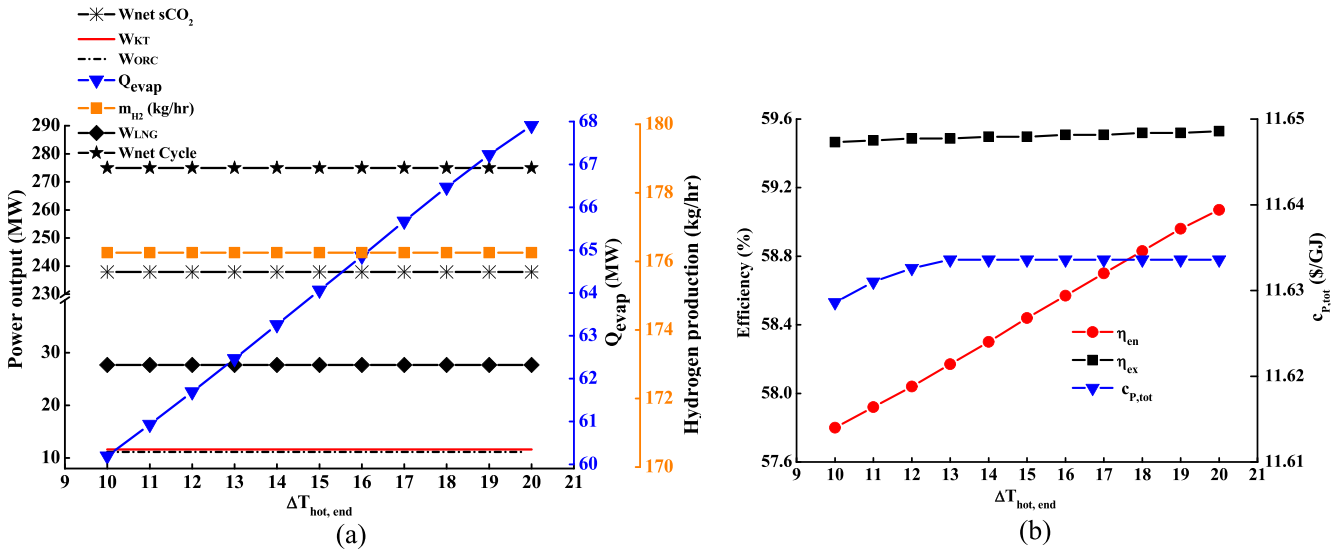


Fig. 8. Impacts of $\Delta T_{gen,hot}$ on: (a) $W_{net,sCO2}$,W_{KT}, W_{ORC}, W_{LNG}, $W_{net,Cycle}$, Q_{evap}, and m_{H2}, and (b) η_{en}, η_{ex} & $c_{p,tot}$.

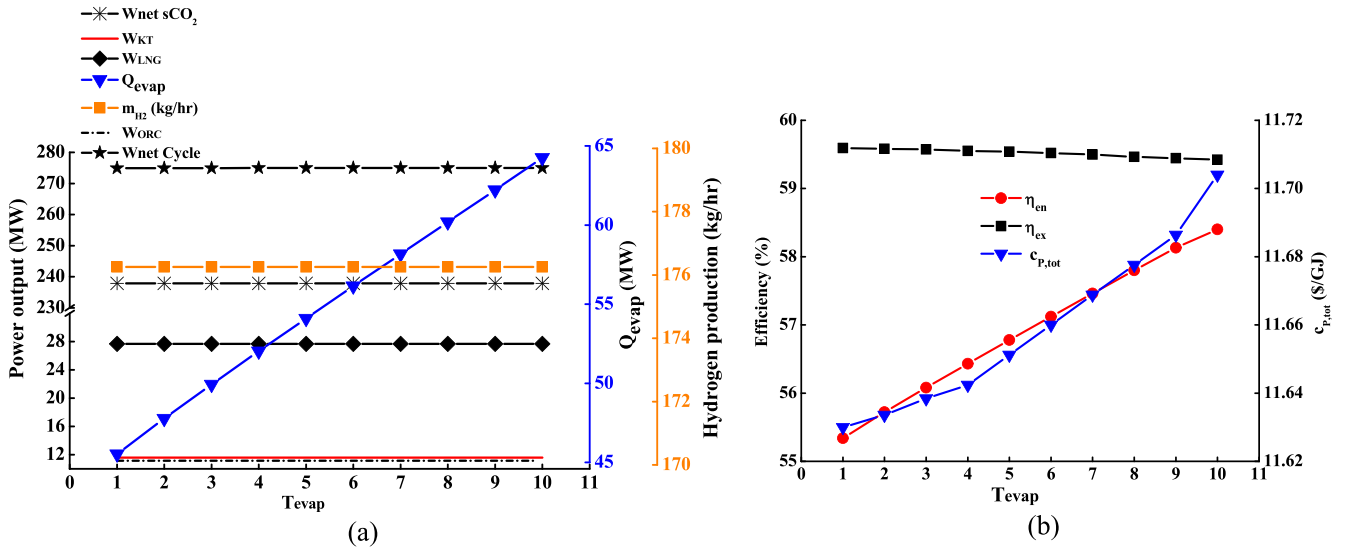


Fig. 9. Impacts of $\Delta T_{gen,hot}$ on: (a) $W_{net,sCO2}$,W_{KT}, W_{ORC}, W_{LNG}, $W_{net,Cycle}$, Q_{evap}, and m_{H2}, and (b) η_{en}, η_{ex} & $c_{p,tot}$.

Table 10
Practical ranges of decision variables.

Decision parameters	PRc	T_2 (°C)	P_{VG1} (KPa)	TTD_{VG1} (°C)	X_{15}	T_{evap} (°C)	$\Delta T_{VG2,hot}$ (°C)
Range	2.4–4.6	500–680	2400–3600	10–20	0.5–0.6	1–10	10–20

temperature subsequently leads to a higher mass flow rate of saturated vapor being released from the separator. However, it also results in a drop in the enthalpy difference across the KC turbine. It's worth noting that the increase in mass flow rate of saturated vapor is nearly offset by the decrease in the enthalpy difference across the KC turbine within the studied TTD_{VG1} range. Consequently, the output power of the KC turbine remains unaltered, depicting a stable trend, as depicted in Fig. 6 (a).

When TTD_{VG1} experiences an increase, it enhances the heat recovery from the CO_2 stream in VG1, consequently leading to a higher mass flow rate of NH_3-H_2O solution circulating in the KC cycle. Conversely, as mentioned earlier, the rise in TTD_{VG1} causes a decrease in separator temperature, which subsequently reduces the temperature and enthalpy of NH_3-H_2O entering HEX4. The observations presented in Fig. 6 (a) demonstrate that as TTD_{VG1} increases, the power output of the ORC also increases. This trend can be ascribed to the fact that the reduction in enthalpy of NH_3-H_2O entering HEX4 is counterbalanced by the increase in the mass flow rate of NH_3-H_2O solution passing through HEX4. Consequently, this leads to a heightened power output in the ORC system. This upsurge in ORC power output, in turn, positively influences the power output of the NG turbine, resulting in a linear increase in the overall system's net power output as TTD_{VG1} increases, as depicted in Fig. 6 (a).

The elevation in TTD_{VG1} enhances heat recovery from the CO_2 stream in VG1, consequently lowering the temperature of the CO_2 stream exiting VG1. This, in turn, decreases the enthalpy of the CO_2 stream entering VG2 within the ARC cycle. The lowered enthalpy, in this

Table 11
Optimization results for both the SCRBC and the proposed trigeneration system.

Parameters	Conventional SCRBC				Proposed tri-generation system			
	Base case	EEOD	XEOD	COD	Base case	EEOD	XEOD	COD
PR	3	4.383	4.383	3.168	3	3.538	4.093	2.901
T_2 (°C)	550	680	680	680	550	680	680	680
P_{VG1} (KPa)	–	–	–	–	3000	3600	3600	3600
TTD_{VG1} (°C)	–	–	–	–	10	10	10	10
X_{15}	–	–	–	–	0.55	0.5	0.5	0.5
T_{evap} (°C)	–	–	–	–	8	10	1	1
$\Delta T_{VG2,hot}$ (°C)	–	–	–	–	10	20	20	10
$W_{net,sCO2}$ (MW)	237.886	270.139	270.139	264.711	237.886	267.856	269.915	261.084
W_{KT} (MW)	–	–	–	–	11.602	11.556	15.423	3.564
W_{ORC} (MW)	–	–	–	–	11.147	9.401	12.325	12.982
W_{LNG} (MW)	–	–	–	–	27.673	24.606	32.156	32.467
$W_{net,\ cycle}$ (MW)	237.886	270.139	270.139	264.711	276.706	300.270	314.396	303.38
$\dot{Q}_{EVAP}$(MW)	–	–	–	–	60.193	73.677	45.816	49.701
m_{H2} (kg/hr)	–	–	–	–	176.25	175.572	219.6	54.108
η_{en}(%)	39.6	45.03	45.03	44.12	57.8	64.47	61.44	59.44
η_{ex}(%)	54.38	62.26	62.26	61.01	59.46	66.24	67.49	61.79
$c_{P,tot}$($/GJ)	12.27	11.07	11.07	10.89	11.642	10.45	10.648	9.869

Table 12
A comparative analysis of the present study and prior research in the field.

References	System	Enhancement in η_{ex} (%)	Enhancement in $c_{P,tot}$ (%)
Current work	Proposed trigeneration system	9.34	5.41
[23]	sCO_2/ARC	2.73	2.03
[45]	sCO_2/ARC + MED	4.02	–
[46]	sCO_2/ORC + ERC	9.17	5.05
[24]	sCO_2/ARC	2.54	–
[47]	sCO_2/KC	6.37	3.51

Table 13
. Formulas for assessing investment costs of system components [25,34,48].

Component	Cost equation	CEPCI
Reactor	$Z_R = C_1 \times \dot{Q}_R,\ C_1 = 283\$/kW_{th}$	402
sCO_2 turbine	$Z_{TUR1} = \left(\frac{479.3\dot{m}_{CO2}}{0.93-\eta_T}\right) \times \ln(PR_c) \times \left(1+e^{(0.036*T_{in}-54.4)}\right)$	368.1
Compressors	$Z_{MC,RC} = \left(\frac{71.1\dot{m}_{CO2}}{0.93-\eta_c}\right) \times PR_c \times \ln(PR_c)$	368.1
Pumps	$Z_{PUMP} = 1120 \times \dot{W}_{PUMP}^{0.8}$	468.2
HTR, LTR	$Z_{HTR,LTR} = 2681 \times A_k^{0.59}$	318.4
KC turbine	$Z_{TUR2} = 4405 \times \dot{W}_{KT}^{0.7}$	368.1
ORC turbine	$Z_{TUR3} = 6000 \times \dot{W}_{ORC}^{0.7}$	368.1
NG turbine	$Z_{TUR4} = 4405 \times \dot{W}_{NG}^{0.7}$	368.1
Generator, Absorber, condenser, SHX, evaporator, and HEXs	$Z_k = Z_{ref,k} \times \left(\frac{A_K}{100}\right)^{0.6}$	394.1
Pre-cooler	$Z_{Pr} = 2143 \times A_k^{0.514}$	318.4
PEME	$Z_{PEME} = 1000 \times \dot{W}_{PEME}$	368.1

Table 14
Coefficients of heat transfer and benchmark costs for components in the system [3].

Component	Heat transfer coefficient (kW/m^2 k)	Reference costs ($)
HTR	3	–
LTR	1.6	–
Pre-cooler	2	–
Absorber	0.8	16,500
Generator	1.3	17,500
Evaporator	1.1	16,000
SHX, HEXs	0.7	12,000
Condenser	0.5	8000

context, diminishes the heat flux in VG2 and reduces the mass flow of refrigerant through the evaporator. The cumulative effect of these changes results in an overall decrease in the cooling load, as indicated in Fig. 6 (a). Additionally, it is essential to emphasize the direct relationship between m_{H2} (hydrogen production) and the power output of the KC system. As depicted in Fig. 6 (a), m_{H2} consistently maintains an unaltered trend as TTD_{VG1} rises.

The findings presented in Fig. 6 (b) reveal that as TTD_{VG1} increases, there is a simultaneous decrease in both the energy and exergy efficiencies within the trigeneration system. This decline can be attributed to the significant reduction in the cooling load, which outweighs the relatively minor increase in output power. Consequently, this adverse effect on efficiencies negatively affects economic aspect of the trigeneration system. As TTD_{VG1} escalates, as visually depicted in Fig. 6 (b), it results in a corresponding increase in the overall product unit cost.

Influence of ammonia concentration (X_{15})

Fig. 7 (a, b) provides a thorough examination of how X_{15} influences the assessment criteria within the proposed tri-generation system. More precisely, Fig. 7 (a) clearly demonstrates that an elevated X_{15} contributes to enhanced power generation from the KC turbine, thereby leading to an augmentation in hydrogen production. This phenomenon is driven by the concurrent rise in the mass flow rate of vapor in a saturated state departing the separator. Although there is a decrease in enthalpy losses across the KC turbine, this drop is surpassed by the augmented mass flow rate, ultimately leading to an overall increase in the power output of the KC turbine.

The findings suggest that an escalation in X_{15} results in a substantial increase in the temperature and enthalpy of NH_3-H_2O when entering HEX4, thereby enhancing the heat recovery from the NH_3-H_2O stream in HEX4 and subsequently improving the power output of the ORC turbine. This increase in ORC power output positively impacts the power output of the NG turbine, resulting in a linear increment in the overall system's net power output, as shown in Fig. 7 (a). Conversely, an elevation in X_{15} causes a decrease in the CO_2 stream temperature exiting VG1. Consequently, this diminishes the enthalpy of the CO_2 stream as it enters VG2 in the ARC cycle, leading to a reduction in the heat flux in VG2 and subsequently a decrease in the cooling load, as depicted in Fig. 7 (a).

As X_{15} increases, a noteworthy trend emerges: the reduction in cooling capacity outweighs the gains in power output and hydrogen production, resulting in a decrease in energy efficiency, as illustrated in

Table 15
. Thermodynamic characteristics and exergy stream costs in the proposed trigeneration system.

State	Fluid	P (kPa)	T (°C)	$\dot{m}$(kg/s)	h (kJ/kg)	s (kJ/kg.K)	X (%)	Y (%)	$\dot{E}$(MW)	Costs	
										$\dot{C}$($/h)	c ($/GJ)
1	CO_2	22,200	385.2	2940	322.8	−0.2968	–	–	1208	48,113	11.06
2	CO_2	22,200	550	2940	526.8	−0.02022	–	–	1569	57,492	10.18
3	CO_2	7400	420.1	2940	384.8	0.002764	–	–	1132	41,472	10.18
4	CO_2	7400	282.2	2940	227.9	−0.2493	–	–	888.1	32,533	10.18
5	CO_2	7400	138.3	2940	64.49	−0.5901	–	–	701.3	25,689	10.18
5a	CO_2	7400	138.3	2144	64.49	−0.5901	–	–	511.5	18,736	10.18
5b	CO_2	7400	138.3	796	64.49	−0.5901	–	–	189.8	6953	10.18
6	CO_2	7400	107.3	2144	26.97	−0.6849	–	–	490.6	17,973	10.18
7	CO_2	7400	107.1	2144	26.72	−0.6856	–	–	490.5	17,968	10.18
8	CO_2	7400	87.71	2144	1.398	−0.7539	–	–	479.2	17,554	10.18
9	CO_2	7400	64.5	2144	–32.83	−0.8521	–	–	467.5	17,125	10.18
10	CO_2	7400	35	2144	−104.4	−1.076			454.6	16,652	10.18
11	CO_2	22,200	115.2	2144	−58.23	−1.058	–	–	542.3	21,510	11.02
12	CO_2	22,200	260.4	2940	165.9	−0.5613	–	–	974.5	39,150	11.16
12a	CO_2	22,200	260.4	2144	165.9	−0.5613	–	–	710.8	28,392	11.1
12b	CO_2	22,200	260.4	796	165.9	−0.5613	–	–	263.8	10,758	11.33
13	Water	101.3	25	1468	104.9	0.3672	–	–	0.2608	0	0
14	Water	101.3	50	1468	209.4	0.7038	–	–	8.825	498.6	15.69
15	NH_3-H_2O	3000	128.3	191.6	636	2.304	0.55	–	2144	103,204	13.37
16	NH_3-H_2O	3000	128.3	44.83	1553	4.62	0.9455	–	863.3	41,562	13.37
17	NH_3-H_2O	461.7	50.16	44.83	1295	4.71	0.9455	–	850.5	40,947	13.37
18	NH_3-H_2O	3000	128.3	146.7	355.8	1.597	0.4292	–	1280	61,642	13.37
19	NH_3-H_2O	3000	40.35	146.7	−54.4	0.45	0.4292	–	1269	61,109	13.37
20	NH_3-H_2O	461.7	40.6	146.7	−54.4	0.4555	0.4292	–	1267	61,109	13.37
21	NH_3-H_2O	461.7	47.28	191.6	261.3	1.453	0.55	–	2120	102,055	13.37
22	NH_3-H_2O	461.7	30	191.6	−101.8	0.2914	0.55		2115	101,847	13.37
23	NH_3-H_2O	3000	30.35	191.6	−98.07	0.2932	0.55	–	2116	101,895	13.38
24	NH_3-H_2O	3000	97.71	191.6	216.1	1.227	0.55	–	2124	102,432	13.4
25	Isobutane	362	26.12	149	590	2.312	–	–	7.579	1787	65.49
26	Isobutane	36.56	−30.43	149	515.2	2.346	–	–	5.081	1198	65.49
27	Isobutane	36.56	−35	149	122.6	0.6979	–	–	8.381	1976	65.49
28	Isobutane	362	−34.86	149	123.2	0.6983	–	–	8.456	1998	65.61
29	LNG	101.3	−161.5	110	−911	−6.677	–	–	115.3	5643	13.6
30	LNG	3000	−160.4	110	−902.9	−6.667	–	–	115.8	5817	13.95
31	NG	3000	−95.88	110	−371	−3.339	–	–	67.05	8992	37.25
32	NG	3000	87.14	110	122.7	−1.365	–	–	57.74	9408	45.25
33	NG	450	−31.45	110	−128.9	−1.246	–	–	36.24	4275	45.25
34	LiBr-H_2O	1.073	33	190	72.15	0.2139	–	52.72	0.2663	21.24	22.15
35	LiBr-H_2O	5.035	33.1	190	72.37	0.2146	–	52.72	0.2689	18.16	18.76
36	LiBr-H_2O	5.035	61.5	190	132.8	0.4018	–	52.72	1.327	162.1	33.94
37	LiBr-H_2O	5.035	77.71	164.7	192.1	0.4349	–	60.82	1.954	241.8	34.37
38	LiBr-H_2O	5.035	41.13	164.7	122.4	0.2267	–	60.82	0.5183	64.13	34.37
39	LiBr-H_2O	1.073	41.13	164.7	122.4	0.2267	–	60.82	0.5183	64.13	34.37
40	Water	5.035	77.71	25.3	2646	8.65	–	–	2.892	360.9	34.67
41	Water	5.035	8	25.3	138.3	0.4779	–	–	0.0279	3.485	34.67
42	Water	1.073	8	25.3	138.3	0.4936	–	–	0.0881	3.485	10.99
43	Water	1.073	25	25.3	2516	8.949	–	–	2.625	103.9	10.99
44	Water	101.3	30	3356	104.9	0.3672	–	–	0.6317	0	0
45	Water	101.3	15	3356	125.8	0.4367	–	–	2.415	200.1	23.02
46	Water	101.3	10	2872	63.08	0.2244	–	–	0.4914	27.59	15.6
47	Water	101.3	25	2872	42.12	0.1511	–	–	2.042	114.7	15.6
48	Water	101.3	30	3038	104.9	0.3672	–	–	0.5718	0	0
49	Water	101.3	25	3038	125.8	0.4367	–	–	2.186	361.4	45.93
50	Water	101.3	25	0.437	104.9	0.3672	–	–	0.00044	0	0
51	Water	101.3	80	0.437	335.1	1.076	–	–	0.0534	4.621	24.06
52	H_2	101.3	80	0.04896	4723	55.86	–	–	0.0039	351.2	25,034
53	O_2	101.3	80	0.3883	50.7	6.56	–	–	0.00239	361.8	41,988

Fig. 7 (b). Surprisingly, the same figure reveals an unexpected observation, although the system's net output power increases more than the decrease in cooling exergy, exergy efficiency follows a declining trend. This intriguing phenomenon can be traced back to the heightened exergy input ($\dot{E}29$-$\dot{E}33$) to the LNG stream due to a significant increase in heat recovery from HEX5, ultimately leading to a decrease in exergy efficiency. Furthermore, the results from the cost analysis shed light on another facet of this trend. The overall cost of the proposed trigeneration system rises as X_{15} increases, aligning with the diminishing exergy efficiency trend. This increase in cost is attributed to the system's declining exergy efficiency, which has implications for its economic viability.

Influence of hot end terminal temperature difference in VG2 ($\Delta T_{gen2,\ hot}$)

Fig. 8 (a, b) provides a comprehensive insight into the impact of $\Delta T_{gen,hot}$ on the key performance parameters that characterize the trigeneration system. The $\Delta T_{gen,hot}$ is defined as $\Delta T_{gen,hot} = T_8 - T_{gen}$. By increasing $\Delta T_{gen,hot}$ while keeping the temperature of CO_2 entering VG2 (T_8) constant, the generator temperature decreases, thereby enhancing heat exchange within the generator. As a result, heat absorption by the ARC generator increases, leading to higher refrigerant mass flow rate and subsequent enhancement in cooling capacity, as demonstrated in Fig. 8 (a). Additionally, Fig. 8 (a) reveals that changing $\Delta T_{gen,hot}$ does not affect the power generation output of KC, ORC, and NG turbines, but it causes a marginal decrease in the net power output of the

trigeneration system, primarily due to a slight increase in pump 4 power within the ARC.

The system's response to the varying $\Delta T_{gen,hot}$ becomes evident in Fig. 8 (b). As $\Delta T_{gen,hot}$ increases, the trigeneration system exhibits a interesting behavior. Despite a marginal reduction in net power output, the increase in cooling load effectively compensates for it, resulting in a notable enhancement in energy efficiency, as illustrated in the figure. Similarly, exergy efficiency shows a slight but significant improvement, primarily attributed to the modest increase in cooling exergy relative to the increase in cooling energy, as visually presented in the graph. Furthermore, the influence of $\Delta T_{gen,hot}$ on the system's cost aspect is worth noting. Initially, there is a slight increase in total investment cost as $\Delta T_{gen,hot}$ varies. However, this increase stabilizes over different $\Delta T_{gen,hot}$ values, ultimately remaining constant.

Influence of evaporator temperature (T_{eva})

Fig. 9 (a-b) provides a detailed examination of how the evaporator temperature (T_{eva}) influences various assessment parameters in the proposed tri-generation system. This analysis reveals the significant role of T_{eva} within the ARC subsystem, particularly in relation to the cooling load, while the power generation of the other subsystems remains largely unaffected. The impact of increasing T_{eva} has a dual effect. Firstly, this temperature elevation enhances the heat input to the ARC, leading to an increased mass flow rate from VG2. This intricate relationship is visually represented in Fig. 9 (a), highlighting the notable increase in cooling output. Concurrently, the rise in T_{eva} results in a reduction in the mass flow rate of the saturated liquid passing through the ARC pump. Consequently, the power consumption of the ARC pump decreases, ultimately resulting in marginal improvements in net power output generation.

An increase in thermal efficiency is observed as the T_{eva} rises. This increase is attributed to the augmented cooling load. However, the analysis of exergy efficiency reveals an interesting finding. Despite the higher cooling load, there is a decrease in exergy efficiency. This occurrence is attributed to the interaction between the variables Q_{eva} and cooling exergy, which are critical components of exergy efficiency. While Q_{eva} exhibits a positive correlation with increasing T_{eva}, cooling exergy, on the other hand, demonstrates a negative relationship. When the positive impact of Q_{eva} on cooling exergy surpasses the negative influence of T_{eva}, cooling exergy increases in conjunction with T_{eva}. Nevertheless, in this particular context, the overall effect of T_{eva} is negative, resulting in a reduction in exergy efficiency, as illustrated in Fig. 9 (b).

When analyzing how T_{eva} variations affect the product cost, it's evident that an increase in T_{eva} leads to a rise in the total investment cost. As a result, the overall cost variation becomes closely associated with the combined impact of net power output and cooling exergy, both of which demonstrate increases, as shown in Fig. 9 (b).

System optimization

To enhance the efficiency of both the conventional SCRBC and our proposed trigeneration system, optimization plays a pivotal role. Our study's primary goal is to optimize these systems by either maximizing energy efficiency (η_{en}) and exergy efficiency (η_{ex}) or minimizing the overall production cost ($c_{P;tot}$). We achieve this optimization by employing the robust genetic algorithm method integrated into the EES software platform. For the SCRBC system, the optimization takes into consideration parameters such as T_2 and PRc as decision variables, while the trigeneration system's optimization encompasses a broader set of parameters, including PRc, T_2, P_{VG1}, TTD_{VG1}, X_{15}, T_{evap}, and $\Delta T_{VG2,hot}$. Table 10 offers detailed constraints for these parameters, while the remaining parameters align with the specifications presented in Table 8.

Table 11 provides a comprehensive overview of the decision parameters and objective function values associated with three different optimization cases: energy efficiency optimal design (EEOD), exergy efficiency optimal design (XEOD), and cost optimal design (COD) scenarios for both the SCRBC and the proposed trigeneration systems. Notably, the optimal pressure ratio (PRc) for the EEOD and XEOD instances in the SCRBC surpasses that of the COD configuration. Comparing the COD situation to the EEOD or XEOD instances for the SCRBC reveals a trade-off: the COD configuration shows a modest 1.652 % reduction in $c_{P;tot}$ but leads to a more significant 2.06 % decrease in energy and exergy efficiencies. Similarly, the COD case in the trigeneration system exhibits a trade-off against the EEOD or XEOD scenarios. In particular, the COD configuration demonstrates a greater reduction of about 5.88 % and 7.89 % in $c_{P;tot}$, resulting in concurrent drops of 8.46 % and 3.36 % in energy efficiency, and 7.2 % and 9.22 % in exergy efficiency, respectively. Contrasting the optimization results between the SCRBC and trigeneration system reveals a consistent trend: the incorporation of the KC-ORC-LNG-PEME-ARC subsystems consistently enhances all three objective functions. Table 11 showcases substantial enhancement percentages for energy efficiency: approximately 43.17 % for EEOD, 36.44 % for XEOD, and 34.72 % for COD scenarios. Furthermore, the exergy efficiency demonstrates increments of around 6.39 % for EEOD, 8.4 % for XEOD, and 1.3 % for COD scenarios. Conversely, a reduction in $c_{P;tot}$ is observed across all three cases, with decrease percentages of approximately 5.93 % for EEOD, 3.96 % for XEOD, and 10.3 % for COD instances.

The proposed trigeneration system stands out in several notable ways. It not only delivers a remarkable increase in net power output, reaching up to 38.82 MW compared to the SCRBC alone in the base design case, but it also offers exceptional cooling capacity, with a capacity of 60.193 MW. Furthermore, the trigeneration system produces significant amounts of hydrogen through the PEM electrolyzer, reaching up to 176.25 kg/hr at the base design case. It's worth noting that the best favorable results are attained when setting T_2 at 680 °C for both the SCRBC and trigeneration system, confirming the positive influence of elevating T_2 on thermodynamic and exergoeconomic performance, as discussed earlier. However, it is essential to address the material corrosion concerns associated with high temperatures.

Comparison with prior research

To illustrate the excellence of our work, we undertook a comparative analysis between our proposed system and other integrated systems. Our investigation centered on CCP systems or trigeneration systems utilizing nuclear-based modified sCO_2 power cycles, allowing us to draw insightful comparisons with our findings. Our developed system surpasses its predecessors in two pivotal aspects. Firstly, in our analysis, as presented in Table 12, we observed substantial performance enhancements in the proposed system. Notably, the system achieved an impressive 9.34 % increase in exergy efficiency and a significant 5.41 % drop in the cost per unit of the final product, surpassing many prior investigations in the field. Furthermore, the current study underscores a firm commitment to sustainability, as demonstrated by our achievement of a remarkably low total product unit cost at 11.64 $/GJ through exergoeconomic analysis. This dedicated emphasis on cost-efficiency corresponds with sustainable principles, facilitating enhanced resource utilization, reduced environmental footprint, and a decreased waste generation. As a result, our proposed system serves as a more eco-friendly and sustainable alternative. Furthermore, we extended our comparative analysis by juxtaposing our proposed trigeneration system with the findings of Toker et al. [43] and Khanmohammadi et al. [44]. In their respective studies, they investigated solar power-assisted integrated trigeneration systems employing sCO_2 cycles as the prime mover. The comparison revealed that our proposed system displayed superior energy and exergy performance compared to these previous studies.

Conclusions

In this study, a novel trigeneration system characterized by high

performance and cost-efficiency is introduced. This system leverages a sCO_2 Brayton cycle as the primary mover and utilizes LNG as a heat sink, thereby enabling simultaneous production of electricity, cooling, and hydrogen. The integration of the KC and ORC takes advantage of the temperature differential between the high-temperature sCO_2 power cycle and the low-temperature LNG cold source. Additional components, such as a PEME and an ARC, contribute to the overall efficiency of this trigeneration system. The viability of the proposed trigeneration system is rigorously evaluated through comprehensive energy, exergy, and exergoeconomic analyses, which serve as pivotal tools for assessing system performance. A parametric exploration is carried out to assess how crucial parameters affect the system's performance. Furthermore, an optimization process using a genetic algorithm (GA) is executed with the objective of maximizing energy efficiency and exergy efficiency or minimizing the overall product cost. The conclusions drawn from our research findings and discussions are as follows:

- The results indicate that the conventional SCRBC system generates 237.89 MW, while the trigeneration system excels, producing 274.976 MW, marking a significant 15.6 % increase in net power output. Additionally, the trigeneration system efficiently provides 60.193 MW of cooling and yields approximately 176.25 kg/hr of hydrogen.
- In standard design conditions, the standalone SCRBC system achieves energy and exergy efficiencies of 39.6 % and 54.38 %, respectively. In contrast, the proposed trigeneration system outperforms with energy and exergy efficiencies of 54.38 % and 59.46 %, demonstrating significant enhancements of 37.3 % and 9.34 %, respectively.
- Moreover, the implementation of the trigeneration system results in a substantial drop in the total product unit cost of the SCRBC system. The cost per unit decreases from $12.272/GJ to a more cost-effective $11.642/GJ, representing a noteworthy 5.41 % cost reduction.
- Comparing the optimization results between the SCRBC and trigeneration systems consistently reveals enhancements in all three performance criteria. Energy efficiency exhibits significant increases, with around 43.17 % for EEOD, 36.44 % for XEOD, and 34.72 % for COD scenarios. Exergy efficiency also sees gains of about 6.39 % for EEOD, 8.4 % for XEOD, and 1.3 % for COD scenarios. Conversely, there is a reduction in total cost ($c_{P;tot}$) across all three cases, with decrease percentages of approximately 5.93 % for EEOD, 3.96 % for XEOD, and 10.3 % for COD instances.
- Future research should employ multi-objective optimization to thoroughly analyze and optimize the proposed system, considering trade-offs between energy and exergy efficiency, along with product cost, to ensure a well-rounded system evaluation.

CRediT authorship contribution statement

Mohamed S. Yousef: Conceptualization, Formal analysis, Funding acquisition, Investigation, Methodology, Project administration, Validation, Writing – original draft, Writing – review & editing. **Domingo Santana:** .

Declaration of competing interest

The authors declare that they have no known competing financial interests or personal relationships that could have appeared to influence the work reported in this paper.

Data availability

Data will be made available on request.

Acknowledgments

The researcher (Mohamed S. Yousef) acknowledges support from the CONEX-Plus program funded by Universidad Carlos III de Madrid and the European Union's Horizon 2020 research and innovation program under the Marie Sklodowska-Curie grant agreement No. 801538.

Appendix A

It is essential to carefully choose the cost functions for each component to accurately compute the expenses in the exergoeconomic analysis. The specifics of the cost functions are outlined in Table A1. It is important to highlight that the cost of the valves, mixer, and separator have been omitted from consideration due to their considerably lower values. Furthermore, the economic data at hand solely comprises formulas that were developed in the past. To enhance comparability, the cost of individual components is adjusted from their original years to a uniform year, employing the chemical engineering plant cost index (CEPCI), as indicated by the following expression [3]:

$$Cost\ in\ current\ year = Original\ year\ cost\ *[(Cost\ index\ for\ current\ year)/\ (Cost\ index\ for\ original\ year)] \quad (A.1)$$

The CEPCI value for the original year is provided in Table A1, with the average CEPCI for the year 2022 being 816.0 [3].

Moreover, in the thermoeconomic analysis, it is imperative to compute the area of each heat exchanger. In this investigation, the equation below is employed to determine the surface area for heat transfer in each heat exchanger [3]:

$$A_k = \frac{Q_k}{U_k \cdot LTMD_k} \quad (A.2)$$

Here, $LTMD_k$ represents the logarithmic mean temperature difference, and U_k denotes the overall heat transfer coefficient, sourced from pertinent literature and consolidated in Table A2 [3].

Table A3 provides an intricate breakdown of the properties associated with each stream within the proposed system. This detailed exposition covers a wide range of thermodynamic and thermoeconomic parameters, all of which are indispensable for a meticulous assessment of the system's overall efficiency.

References

[1] Soliman AMA, Yousef MS, Ookawara S, Hassan H. Experimental study of using system of flat heat pipe-phase change material inclusion heat sink for thermal regulation of simulated PV. Exp Heat Transf 2023;36:648–64. https://doi.org/10.1080/08916152.2022.2071359.

[2] Sun R, Liu M, Chen X, Yang K, Yan J. Thermodynamic optimization on supercritical carbon dioxide Brayton cycles to achieve combined heat and power generation. Energy Convers Manag 2022;251:114929. https://doi.org/10.1016/j.enconman.2021.114929.

[3] Tang J, Zhang Q, Zhang Z, Li Q, Wu C, Wang X. Development and performance assessment of a novel combined power system integrating a supercritical carbon dioxide Brayton cycle with an absorption heat transformer. Energy Convers Manag 2022;251:114992. https://doi.org/10.1016/j.enconman.2021.114992.
[4] Tiktas A, Gunerhan H, Hepbasli A. Single and multigeneration Rankine cycles with aspects of thermodynamical modeling, energy and exergy analyses and optimization: a key review along with novel system description figures. Energy Convers Manag X 2022;14:100199. https://doi.org/10.1016/j.ecmx.2022.100199.
[5] Tsimpoukis D, Syngounas E, Bellos E, Koukou M, Tzivanidis C, Anagnostatos S, et al. Thermodynamic and economic analysis of a supermarket transcritical CO2 refrigeration system coupled with solar-fed supercritical CO2 Brayton and organic Rankine cycles. Energy Convers Manag X 2023;18:100351. https://doi.org/10.1016/j.ecmx.2023.100351.
[6] Song J, Li Xs, Ren Xd, Gu Cw. Performance analysis and parametric optimization of supercritical carbon dioxide (S-CO2) cycle with bottoming Organic Rankine Cycle (ORC). Energy 2018;143:406–16. https://doi.org/10.1016/j.energy.2017.10.136.
[7] Wu C, Wang S, Li J. Exergoeconomic analysis and optimization of a combined supercritical carbon dioxide recompression Brayton / organic fl ash cycle for nuclear power plants. Energy Convers Manag 2018;171:936–52. https://doi.org/10.1016/j.enconman.2018.06.041.
[8] Wang X, Dai Y. Exergoeconomic analysis of utilizing the transcritical CO2 cycle and the ORC for a recompression supercritical CO2 cycle waste heat recovery: a comparative study. Appl Energy 2016;170:193–207. https://doi.org/10.1016/j.apenergy.2016.02.112.
[9] Kojur NB, Namdar M, Nasero MJ, Aminian S, Koosha N, Zarei K. Energy, exergy, economic, and exergoeconomic analyses and optimization of a solar Kalina cycle using particle swarm optimization algorithm. Energy Convers Manag X 2023;18:100372. https://doi.org/10.1016/j.ecmx.2023.100372.
[10] Dhahad HA, Hussen HM, Nguyen PT, Ghaebi H, Ashraf MA. Thermodynamic and thermoeconomic analysis of innovative integration of Kalina and absorption refrigeration cycles for simultaneously cooling and power generation. Energy Convers Manag 2020;203:112241. https://doi.org/10.1016/j.enconman.2019.112241.
[11] Shokati N, Ranjbar F, Yari M. Exergoeconomic analysis and optimization of basic, dual-pressure and dual-fluid ORCs and Kalina geothermal power plants: a comparative study. Renew Energy 2015;83:527–42. https://doi.org/10.1016/j.renene.2015.04.069.
[12] Li H, Wang M, Wang J, Dai Y. Exergoeconomic analysis and optimization of a supercritical CO2 cycle coupled with a Kalina cycle. J Energy Eng 2017;143:1–13. https://doi.org/10.1061/(asce)ey.1943-7897.0000411.
[13] Mahmoudi SMS, Akbari AD, Rosen MA. Thermoeconomic analysis and optimization of a new combined supercritical carbon dioxide recompression Brayton/Kalina cycle. Sustain 2016;8. https://doi.org/10.3390/su8101079.
[14] Yuan J, Wu C, Xu X, Liu C. Proposal and thermoeconomic analysis of a novel combined cooling and power system using carbon dioxide as the working fluid. Energy Convers Manag 2021;227:113566. https://doi.org/10.1016/j.enconman.2020.113566.
[15] Yuan J, Wu C, Xu X, Liu C. Multi-mode analysis and comparison of four different carbon dioxide-based combined cooling and power cycles for the distributed energy system. Energy Convers Manag 2021;244:114476. https://doi.org/10.1016/j.enconman.2021.114476.
[16] Li B, Wang Ss. Thermo-economic analysis and optimization of a novel carbon dioxide based combined cooling and power system. Energy Convers Manag 2019;199. https://doi.org/10.1016/j.enconman.2019.112048.
[17] Pan M, Bian X, Zhu Y, Liang Y, Lu F, Xiao G. Thermodynamic analysis of a combined supercritical CO2 and ejector expansion refrigeration cycle for engine waste heat recovery. Energy Convers Manag 2020;224:113373. https://doi.org/10.1016/j.enconman.2020.113373.
[18] Yousef MS, Santana D. Energy and exergy analyses of a recompression supercritical CO2 cycle combined with a double-effect parallel absorption refrigeration cycle. Energy Rep 2023;9:195–201. https://doi.org/10.1016/j.egyr.2023.09.161.
[19] Sadman Bishal S, Imtiaz Anando A, Fahim Faysal D, Monjurul EM. Performance evaluation of a novel multigeneration plant of cooling, power, and seawater desalination using supercritical CO2 partial cooling, ME-TVC desalination, and absorption refrigeration cycles. Energy Convers Manag X 2023;20:100485. https://doi.org/10.1016/j.ecmx.2023.100485.
[20] Ghiasirad H, Asgari N, Khoshbakhti Saray R, Mirmasoumi S. Thermoeconomic assessment of a geothermal based combined cooling, heating, and power system, integrated with a humidification-dehumidification desalination unit and an absorption heat transformer. Energy Convers Manag 2021;235:113969. https://doi.org/10.1016/j.enconman.2021.113969.
[21] Bani Hani EH, Sinaga N, Khanmohammdi S, Diyoke C. Assessment of a waste energy recovery (WER) unit for power and refrigeration generation: advanced thermodynamic examination. Sustain Energy Technol Assessments 2022;52:102213. https://doi.org/10.1016/j.seta.2022.102213.
[22] Li H, Su W, Cao L, Chang F, Xia W, Dai Y. Preliminary conceptual design and thermodynamic comparative study on vapor absorption refrigeration cycles integrated with a supercritical CO2 power cycle. Energy Convers Manag 2018;161:162–71. https://doi.org/10.1016/j.enconman.2018.01.065.
[23] Wu C, Wang Ss, Feng Xj, Li Jj. Energy, exergy and exergoeconomic analyses of a combined supercritical CO2 recompression Brayton/absorption refrigeration cycle. Energy Convers Manag 2017;148:360–77. https://doi.org/10.1016/j.enconman.2017.05.042.
[24] Wu C, Xu X, Li Q, Li J, Wang S, Liu C. Proposal and assessment of a combined cooling and power system based on the regenerative supercritical carbon dioxide Brayton cycle integrated with an absorption refrigeration cycle for engine waste heat recovery. Energy Convers Manag 2020;207:112527. https://doi.org/10.1016/j.enconman.2020.112527.
[25] Li J, Zoghi M, Zhao L. Thermo-economic assessment and optimization of a geothermal-driven tri-generation system for power, cooling, and hydrogen production. Energy 2022;244:123151. https://doi.org/10.1016/j.energy.2022.123151.
[26] Liang W, Yu Z, Bai S, Li G, Wang D. Study on a near-zero emission SOFC-based multi-generation system combined with organic Rankine cycle and transcritical CO2 cycle for LNG cold energy recovery. Energy Convers Manag 2022;253:115188. https://doi.org/10.1016/j.enconman.2021.115188.
[27] Ebadollahi M, Rostamzadeh H, Pedram MZ, Ghaebi H, Amidpour M. Proposal and assessment of a new geothermal-based multigeneration system for cooling, heating, power, and hydrogen production, using LNG cold energy recovery. Renew Energy 2019;135:66–87. https://doi.org/10.1016/j.renene.2018.11.108.
[28] Ghaebi H, Namin AS, Rostamzadeh H. Exergoeconomic optimization of a novel cascade Kalina/Kalina cycle using geothermal heat source and LNG cold energy recovery. J Clean Prod 2018;189:279–96. https://doi.org/10.1016/j.jclepro.2018.04.049.
[29] Chitgar N, Moghimi M. Design and evaluation of a novel multi-generation system based on SOFC-GT for electricity, fresh water and hydrogen production. Energy 2020;197:117162. https://doi.org/10.1016/j.energy.2020.117162.
[30] Abid M, Khan MS, Ratlamwala TAH. Comparative energy, exergy and exergo-economic analysis of solar driven supercritical carbon dioxide power and hydrogen generation cycle. Int J Hydrogen Energy 2020;45:5653–67. https://doi.org/10.1016/j.ijhydene.2019.06.103.
[31] Hadelu LM, Noorpoor A, Boyaghchi FA, Mirjalili S. Exergoeconomic, carbon, and water footprint analyses and optimization of a new solar-driven multigeneration system based on supercritical CO2 cycle and solid oxide steam electrolyzer using various phase change materials. Process Saf Environ Prot 2022;159:393–421. https://doi.org/10.1016/j.psep.2022.01.013.
[32] Klein S, Alvarado F. Engineering equation solver. F-Chart Software, Box 2002:1–2.
[33] Sharaf M, Yousef MS, Huzayyin AS. Year-round energy and exergy performance investigation of a photovoltaic panel coupled with metal foam/phase change material composite. Renew Energy 2022. https://doi.org/10.1016/j.renene.2022.03.071.
[34] Yousef MS, Santana D. Thermodynamic and exergoeconomic optimization of a new combined cooling and power system based on supercritical CO2 recompression Brayton cycle. Energy Convers Manag 2023;295:117592. https://doi.org/10.1016/j.enconman.2023.117592.
[35] Emadi MA, Mahmoudimehr J. Modeling and thermo-economic optimization of a new multi-generation system with geothermal heat source and LNG heat sink. Energy Convers Manag 2019;189:153–66. https://doi.org/10.1016/j.enconman.2019.03.086.
[36] Yousef MS, Santana D. Thermodynamic and Exergoeconomic Analysis of Utilizing a Modified Kalina Cycle for a Recompression Supercritical CO 2 Cycle Waste Heat Recovery. 2023 6th Int Conf Electr Eng Green Energy 2023:253–9. https://doi.org/10.1109/ceege58447.2023.10246643.
[37] Noaman M, Saade G, Morosuk T, Tsatsaronis G. Exergoeconomic analysis applied to supercritical CO2 power systems. Energy 2019;183:756–65. https://doi.org/10.1016/j.energy.2019.06.161.
[38] Wang X, Yang Y, Zheng Y, Dai Y. Exergy and exergoeconomic analyses of a supercritical CO2 cycle for a cogeneration application. Energy 2017;119:971–82. https://doi.org/10.1016/j.energy.2016.11.044.
[39] Hettiarachchi HDM, Golubovic M, Worek WM, Ikegami Y. The performance of the Kalina cycle system 11(kcs-11) with low-temperature heat sources. J Energy Resour Technol Trans ASME 2007;129:243–7. https://doi.org/10.1115/1.2748815.
[40] Chacartegui R, Sánchez D, Muñoz JM, Sánchez T. Alternative ORC bottoming cycles FOR combined cycle power plants. Appl Energy 2009;86:2162–70. https://doi.org/10.1016/j.apenergy.2009.02.016.
[41] Kerme ED, Chafidz A, Agboola OP, Orfi J, Fakeeha AH, Al-Fatesh AS. Energetic and exergetic analysis of solar-powered lithium bromide-water absorption cooling system. J Clean Prod 2017;151:60–73. https://doi.org/10.1016/j.jclepro.2017.03.060.
[42] Ioroi T, Yasuda K, Siroma Z, Fujiwara N, Miyazaki Y. Thin film electrocatalyst layer for unitized regenerative polymer electrolyte fuel cells. J Power Sources 2002;112:583–7. https://doi.org/10.1016/S0378-7753(02)00466-4.
[43] Toker SC, Soyturk G, Kizilkan O. Development of a sustainable multi-generation system with re-compression sCO2 Brayton cycle for hydrogen generation. Int J Hydrogen Energy 2022;47:19397–410. https://doi.org/10.1016/j.ijhydene.2021.11.138.
[44] Khanmohammadi S, Kizilkan O, Musharavati F. ScienceDirect Comparative analyses of a novel solar tower assisted multi-generation system with re-compression CO 2 power cycle, thermoelectric generator, and hydrogen production unit. Int J Hydrogen Energy 2022;47:25984–99. https://doi.org/10.1016/j.ijhydene.2022.04.082.
[45] Li HW, Sun Y, Pan YY, Du CH, Wang D. Preliminary design, thermodynamic analysis and optimization of a novel carbon dioxide based combined power, cooling and distillate water system. Energy Convers Manag 2022;255:115367. https://doi.org/10.1016/j.enconman.2022.115367.
[46] Fan G, Li H, Du Y, Zheng S, Chen K, Dai Y. Preliminary conceptual design and thermo-economic analysis of a combined cooling, heating and power system based

on supercritical carbon dioxide cycle. Energy 2020;203:117842. https://doi.org/10.1016/j.energy.2020.117842.

[47] Fan G, Dai Y. Thermo-economic optimization and part-load analysis of the combined supercritical CO2 and Kalina cycle. Energy Convers Manag 2021;245:114572. https://doi.org/10.1016/j.enconman.2021.114572.

[48] Azariyan H, Vajdi M, Rostamnejad TH. Assessment of a high-performance geothermal-based multigeneration system for production of power, cooling, and hydrogen: thermodynamic and exergoeconomic evaluation. Energy Convers Manag 2021;236:113970. https://doi.org/10.1016/j.enconman.2021.113970.